

THIN AND THICK STELLAR DISKS IN NGC 551

MS (Research) Thesis

By:

Harshal Raut



**DEPARTMENT OF ASTRONOMY, ASTROPHYSICS AND
SPACE ENGINEERING**

INDIAN INSTITUTE OF TECHNOLOGY INDORE

June, 2025

THIN AND THICK STELLAR DISKS IN NGC 551

A THESIS

*Submitted in partial fulfillment of the
requirements for the award of the degree
of*

Master of Science (Research)

by

Harshal Raut




**DEPARTMENT OF ASTRONOMY, ASTROPHYSICS AND
SPACE ENGINEERING**

INDIAN INSTITUTE OF TECHNOLOGY INDORE

June, 2025

INDIAN INSTITUTE OF TECHNOLOGY INDORE
CANDIDATE'S DECLARATION

I hereby certify that the work which is being presented in the thesis entitled "**Thin and Thick Stellar Disks in NGC 551**" in partial fulfillment of the requirements for the award of the degree of MASTER OF SCIENCE (RESEARCH) and submitted in the DEPARTMENT OF ASTRONOMY, ASTROPHYSICS AND SPACE ENGINEERING, Indian Institute of Technology Indore, is an authentic record of my own work carried out during the time period from July 2022 to July 2024 under the supervision of Dr. Narendra Nath Patra, Assistant Professor in IIT Indore. The matter presented in this thesis has not been submitted by me for the award of any other degree of this or any other institute.


Signature with date 30/06/25
(Harshal Raut)

This is to certify that the above statement made by the candidate is correct to the best of my knowledge.

Signature of the Supervisor of

M.S(Research) Thesis

(Dr.Narendra Nath Patra)

Narendra Nath Patra .
30.06.2025 .

Harshal Raut has successfully given his M.S (Research) Oral Examination held on

27/06/25

Somnath Dey 30/6/25
Signature(s) of Chairperson(OEB)

Date:

Soumaro Ghosh
Signature of Convener, DPGC

Date:- 30/06/25

Signature of Thesis

Supervisor Narendra Nath Patra .

Date:- 30.06.2025 .

Signature of Head of Discipline

Date:- 30.06.2025 Narendra Nath Patra .
(officiating)
Head

ACKNOWLEDGEMENTS

I am immensely thankful to everyone who has supported and contributed to the culmination of this thesis. Their steadfast support, guidance, and encouragement have been incredibly valuable throughout this journey. Foremost, I would like to extend my heartfelt appreciation to my supervisor, Dr. Narendra Nath Patra, for their continuous guidance, mentorship, and expertise. Their patience, encouragement, and insightful feedback have been instrumental in shaping the direction and quality of this thesis. I am also grateful to the PSPCs members of my thesis committee, Dr. Manoneeta Chakraborty and Dr. Onkar Game, for their valuable inputs, suggestions, and constructive criticisms that have enriched the content and quality of this thesis.

I thank C.A. Narayan and C.J. Jog, whose published work has been a foundation for this particular project. I can't thank my family enough for their constant support. I wish to express my gratitude to my friends and fellow lab mates for their engaging discussions, technical guidance, and unwavering moral support. Their camaraderie and uplifting spirit have been a driving force, motivating and inspiring me throughout this endeavor. Finally, I want to convey my appreciation to all the researchers, scholars, and authors whose work I have cited and referred to throughout this thesis. Their contributions have significantly enhanced the academic dialogue and played a crucial role in forming the theoretical and conceptual foundation of this research.

ABSTRACT

The Milky Way contains two stellar disks: a thin disk extending to a height of a few hundred parsecs and a thick disk extending to a height of a few kiloparsecs. Understanding galactic structure helps us comprehend the evolutionary processes that shaped the galaxy into its current form.

The vertical stability of a galactic disk depends on the balance between gravitational forces and pressure gradients. Theoretically, the disk's vertical structure can be calculated by solving the coupled Poisson-Jeans equations. The gravitational component is interpreted through observed mass (from optical and radio observations), while pressure is estimated from observed velocity dispersion. Within the galactic disk, stellar mass contributes significantly to the total mass, which is balanced by stellar velocity dispersion. Therefore, solving the Poisson-Jeans equations requires information about both stellar surface density and velocity dispersion.

However, due to limited spectroscopic data across the entire optical disks, earlier studies calculated stellar velocity dispersion through analytical methods. In this work, we utilize Integral Field Unit data to estimate velocity dispersion in stellar disks and quantify how this approach changes the density structure compared to analytically calculated velocity dispersions. Using these parameters, we solved the coupled Poisson-Jeans equations and constructed a galactic model using the density solutions.

We compared observational maps with surface brightness maps produced by our model. At all heights except the center, our model closely matches observations. The observed center shows a spike-like component that is absent in our model. We determined that NGC 551's emission is consistent with a thin disk structure. To verify whether the spike-like emission originates solely from the thin disk rather than other components, we constructed two additional models: a thin-plus-thick stellar disk model and a bar-plus-thick disk model. The vertical slices across the moment-0 maps of these models do not match the observational slices, supporting the conclusion that the emission arises from the thin disk.

We further used our dynamical model to generate a simulated edge-on surface brightness map of the stellar disk. We fitted this map using a modified Bessel function of the first kind and a sech^2 function to estimate the apparent disk parameters. This fitting process artificially reduces both the scale length and the disk's flattening ratio compared to parameter values obtained through detailed modeling. Examining the model's edge-on vertical profiles at different radii, we found that a double Gaussian provides a better fit than a single Gaussian. This suggests that a two-component disk structure artificially emerges in edge-on surface brightness distributions due to line-of-sight projection effects. Therefore, detailed modeling is essential to confirm the existence of multi-component stellar disks in external galaxies.

Contents

1	Introduction	1
2	Hydrostatic Equilibrium	8
2.1	Equation of Hydrostatic Equilibrium	10
2.2	Input Parameters to the Differential Equation	12
2.2.1	Surface Densities	12
2.2.2	Velocity Dispersion	17
2.2.3	Rotation Curve	20
2.2.4	Dark Matter Halo Profile	22
2.2.5	Solving the Hydrostatic Equation	24
3	Results and Discussion	26
3.1	σ_* Profile	27
3.2	Three-dimensional density distribution in the stellar disk	29
3.3	Two-component (thin+thick) stellar disk in NGC 551?	31
3.4	Multi Component Models	34
3.4.1	Thick + Thin Model	34
3.4.2	Thick + Bar Model	37
3.5	Edge-On Models	40
3.6	Plausible Formation Scenarios of Thick Stellar Disk	44
3.6.1	Radial Migration	44
3.6.2	Bars	45
3.6.3	GMCs	46
3.6.4	Stellar Clumps	46

4 Conclusions and Scope for Future Work

48

REFERENCES

List of Figures

1.1	NGC 551 observed in R-band	7
1.2	NGC 551 observed in 3.6 μm	7
2.1	The MGE fit of NGC 551. The black contours represent the observed stellar surface brightness distribution, whereas the MGE-fitted contours to the isophotes are shown in red.	13
2.2	The Σ_{H_2} distribution in NGC 551. The white ellipse shows a representative annular region (a radial bin) at a radius of 6 kpc over which Σ_{H_2} was averaged to obtain a data point in the Σ_{H_2} profile. The red dashed line designates the major axis of the galaxy.	14
2.3	The deprojected surface density profiles of different disks in NGC 551. The solid blue line represents the stellar surface density, whereas the dashed orange and dashed-dotted green lines represent the molecular and atomic gas surface density profiles, respectively. Error bars reflect formal 1σ uncertainties in the stellar surface density.	15
2.4	Stellar velocity dispersion map of NGC 551 from the third data release of the CALIFA survey. A velocity dispersion profile is generated by averaging velocity dispersion values in annular rings at different radial bins. The white elliptical region shows one such bin at 6 kpc. The red dashed line designates the major axis of the galaxy.	19

2.5	Rotation curve of NGC 551 derived from the HI spectral cube. The red circles with error bars represent the rotation curve, whereas the black dashed line signifies a fit to the rotation curve with a Brandt profile	21
2.6	The iterative method workflow is illustrated. In each panel, the red circles represent the observed MOM2, the blue squares denote the simulated MOM2, whereas the black asterisks indicate the input intrinsic stellar velocity dispersion σ_* . The shaded region represents radii where we do not solve the iterative method. The left panel shows the results for the first iteration, whereas the middle and the right panel show the results for the second and ninth iteration. As can be seen, the iterative method for NGC 551 quickly converges within ten iterations. See the text for more details.	25
3.1	The velocity dispersion profiles of the stellar disk in NGC 551. The orange triangles represent the σ_* as obtained by analytical calculation from Leroy et al. (2008). The blue circles show the σ_* profile as obtained by the iterative method. The green squares show the σ_* profile obtained by the Disk Mass Survey (Bershady et al., 2010b). Error bars reflect formal 1σ uncertainties in the velocity dispersion.	27
3.2	The solutions of the hydrostatic equilibrium equation at a radius of 6 kpc. The left, middle, and right panels present density solutions for stars, molecular, and atomic gas respectively. The solid lines in each panel represent solutions when the hydrostatic equations were solved with the iterative method using CALIFA IFU data. The dashed lines represent the solutions with the analytically calculated stellar velocity dispersion.	30

3.3	The scale height of different baryonic disks in NGC 551 under hydrostatic equilibrium. The left, middle, and right panels represent scale heights for the stellar, molecular, and atomic disks respectively. The solid lines in each panel represent the scale height due to our iterative method, whereas the dashed lines represent the same for our analytically calculated σ_* . The vertical dashed line in the left panel indicates the scale length of the stellar disk (4.6 kpc).	30
3.4	The simulated moment maps of the stellar disk in NGC 551. The left panel shows the moment zero map, i.e., the total surface brightness map in the units of $M_\odot \text{ pc}^{-2}$. The middle panel shows the moment one map or the velocity field of the galaxy. The right panel represents the velocity dispersion map. The last two maps have units of km s^{-1} . These moment maps are generated using the simulated spectral cube obtained through the dynamical modeling of the stellar disk.	31
3.5	Vertical slices taken at different radii to compare the simulation with observation. The left panel represents the surface brightness map of the stellar disk as obtained by IFU observation. The middle panel shows the stellar disk as observed in Spitzer $3.6 \mu\text{m}$ data. The right panel shows our simulated intensity distribution. The crosses in each panel indicate the center of the galaxy. The red and the cyan dashed lines denote the region ($2.5 - 5 \text{ kpc}$) over which the simulation and the observations are compared.	32

3.6	Comparison of vertical slices of the surface density distribution in the stellar disk of NGC 551. In the top panels, we compare the IFU observation with the simulation, whereas in the bottom panels, we compare Spitzer $3.6\ \mu\text{m}$ with the simulation. The different panels represent comparisons at different radii. In each panel, the solid lines denote the simulated vertical slices profiles. Dashed lines show the observed vertical profiles. Two different colors represent two different halves (left and right) of the observed map. As can be seen from the figure, the simulated profiles at different radii match the observations very well, except at the central region.	33
3.7	Comparing model 1 ($27.5\%\Sigma_\star$ for thick disk), model 2 ($10.3\%\Sigma_\star$ for thick disk) and single disk model MOM 0 map vertical slices Σ_\star profile at a radius of 2.5 kpc. The green solid line represents the single disk model. The orange and blue solid lines represent the thick + thin model 1 and model 2 respectively.	35
3.8	Comparing MOM-2 radial profiles for different models with different $\sigma_{\star,\text{tn}}$. The black solid line represents the radial profile as obtained by the CALIFA IFU. The red and blue solid line represents the radial profile as obtained from the simulated MOM-2 maps of model 1 and model 2, respectively.	37
3.9	The left panel shows the 2D bar generated from the Sérsic bar profile. The right panel shows the MOM-0 map of thick disk + bar model of NGC 551.	39

3.10	Comparison of vertical slices of the surface density distribution in the stellar disk of NGC 551. In the top panels, we compare the IFU observation with the bar+thick disk model, whereas in the bottom panels, we compare Spitzer $3.6\ \mu\text{m}$ with the bar+thick disk model. The different panels represent comparisons at different radii. In each panel, the solid lines denote the simulated vertical slices profiles. Dashed lines show the observed vertical profiles. Two different colors represent two different halves (left and right) of the observed map.	40
3.11	The surface brightness map of the stellar disk in NGC 551 in an edge-on orientation. The left panel shows the surface brightness map, whereas the middle panel represents a 2D fit to the map with the modified Bessel Function of the first kind $K(x)$ and a sech^2 . The right panel shows the residual of the fitting. The blanked portion in the middle of each panel represents the region where we do not solve the hydrostatic equilibrium equation. . . .	41
3.12	The estimated flattening ratio of the stellar disk in NGC 551 as a function of radius. The estimation was done using the modeled scale height and the observed scale length of the disk. As can be seen, the flattening ratio varies substantially (between $\sim 10 - 23$) with radius.	42
3.13	The vertical slices profile of the simulated intensity distribution of the stellar disk at an edge-on orientation, and it's fit with single and double Gaussian components. The first two panels show vertical slices at a radius of 2.5 kpc, whereas the last two panels show cuts at 3.5 kpc. The solid black lines represent the vertical slices of the edge-on intensity. The dashed red lines represent the fits. The first and third panels show a single Gaussian fit, whereas the second and fourth panels represent a double Gaussian fit.	43

List of Tables

1.1	Basic properties of NGC 551.	7
2.1	MGEfit parameter of NGC 551	14
2.2	Brandt profile parameters from the fit	21
2.3	Dark Matter Halo Parameters	23
3.1	Best-fit parameters from the Sérsic + exponential disk + Sérsic model	38

Chapter 1

Introduction

The structural and chemical properties of stars in the Galaxy have been extensively studied to understand the nature of the stellar disk. Several spectroscopic surveys have measured the precise chemical and kinematic properties of a large number of stars in the Galaxy ([Luo et al., 2015](#); [Majewski et al., 2017](#); [Buder et al., 2018](#); [Steinmetz et al., 2020](#); [Gaia Collaboration et al., 2021b](#); [Gilmore et al., 2022](#)). These measurements provided unprecedented coverage of the stellar disk, both in terms of their spatial distribution and chemical history. Furthermore, these surveys help to understand the evolutionary history of the stellar disk in the Galaxy.

A thorough analysis of these surveys revealed the presence of a double-component stellar disk within the solar neighborhood of the Milky Way. The stellar disk is found to have a ‘thin’ and a ‘thick’ component (see, e.g., [Gilmore & Reid, 1983](#)). The thin disk has a much smaller scale height, residing close to the midplane, whereas the thick disk has a larger extent in the vertical direction. Furthermore, the thin disk extends farther in the radial direction than the thick disk ([Larsen & Humphreys, 2003](#); [Jurić et al., 2008](#)). The thick disk is characterized by a high vertical velocity dispersion of the stellar component and a slow systemic rotation around the galactic center as compared to the thin disk ([Bensby et al., 2011](#); [Robin et al., 2022](#)). Not only that, the two disks are found to be chemically different as well. The thin disk is metal-rich, comprising young stars, whereas the thick disk is more dominated by metal-poor and old stars, ([Fuhrmann, 1998](#)), indicating most likely that the two disks have different origins

and evolutionary tracks.

In the literature, several different mechanisms have been proposed to explain the existence of thick stellar disks in galaxies. For example, some studies invoke external influences, such as mergers, tidal interactions, etc. (see, e.g., [Brook et al., 2012](#); [Grand et al., 2020](#)), as the primary source of disturbances producing thick disks. At the same time, other studies point toward internal mechanisms, e.g., radial migration induced by resonances, dynamical heating by bulges, interactions with Giant Molecular Clouds (GMCs), disruptive effects of stellar clumps, etc. (see, e.g., [Sellwood & Binney, 2002](#); [Saha et al., 2010](#); [Fujimoto et al., 2023](#); [Bournaud et al., 2009](#)).

Studies have also found the existence of two-component disks in external galaxies. For example, [Yoachim & Dalcanton \(2006\)](#) analyzed the vertical light distribution in 34 edge-on galaxies, fitting the r – band surface brightness distribution from the du Pont 2.5m telescope from the Las Campanas observatory. They found that a two-disk model (thin + thick) is required to explain the observation. Furthermore, [Comerón et al. \(2018\)](#) analyzed the surface brightness of 141 edge-on galaxies using data from the Spitzer Survey of Stellar Structure in Galaxies, the S⁴G survey ([Muñoz-Mateos et al., 2015](#); [Sheth et al., 2010](#)). Out of their 141 galaxies, only the surface brightness distributions of 17 galaxies were best fitted by a single disk component, while the remaining 116 galaxies required a two-disk model and 8 galaxies required a three-disk model to explain the observed surface brightness. In a recent study, [Sattler et al. \(2023\)](#) used Integral-Field spectroscopy data from MUSE ([Bacon et al., 2010](#)) to investigate the stellar kinematics in the edge-on galaxy NGC 3501. They also found that a two-disk model is suitable for explaining the observed kinematics and surface density distribution in this galaxy.

These studies strongly indicate the existence of two-component disks in galaxies, at least identified geometrically and chemically. Nevertheless, observing and measuring three-dimensional density distribution would be a direct confirmation. However, projection effects contaminate such measurements due to line-of-sight integration. For example, even for edge-on galaxies, the volume density distribution can only be determined directly from observation if the scale

height does not change with radius, which has been shown to not always be true. Several authors have shown, theoretically and observationally, that the scale height of galactic disks increases with radius, resulting in flaring ([Narayan & Jog, 2002](#); [Banerjee & Jog, 2007](#); [Patra, 2019, 2020](#)). Also, in the case of a two-component disk, the scale length of the thin and the thick disk could be different ([Bensby et al., 2011](#); [Bovy et al., 2016](#); [Mackereth et al., 2017](#); [Lian et al., 2022](#); [Robin et al., 2022](#); [Imig et al., 2023](#)), complicating the observed edge-on surface densities further.

To tackle these observational issues, many previous studies relied upon theoretical modeling of the galactic disks (see, e.g., [Narayan & Jog, 2002](#); [Banerjee & Jog, 2007](#); [Patra, 2019, 2020](#)). Assuming the galactic disks to be in vertical hydrostatic equilibrium in a gravitationally-coupled multi-component disk, joint Poisson’s equations could be set up and solved to obtain the three-dimensional density distribution. [Patra \(2021\)](#) used this modeling method to identify a two-component molecular disk in the galaxy NGC 6946. In hydrostatic modeling, the vertical velocity dispersion is a vital parameter. It determines the vertical pressure, which balances the gravitational force. In earlier studies, the velocity dispersion in the stellar disks was calculated theoretically due to a lack of spectroscopic observations ([Narayan & Jog, 2002](#)). Several simplified assumptions were employed to calculate stellar velocity dispersion. For example, the stellar disk was assumed to be in vertical hydrostatic equilibrium solely under its gravity (contribution from gas and dark matter neglected) ([Sarkar & Jog, 2020](#)). Stellar scale height was considered to be constant across the galaxy, and it was calculated from a general flattening ratio. However, this flattening ratio can vary from galaxy to galaxy ([Bizyaev et al., 2014](#); [De Geyter et al., 2014](#); [Peters et al., 2017](#)). These assumptions are not true in general, and a direct determination of the stellar velocity dispersion is desirable to model the galactic disks hydrostatically.

A direct measurement of the vertical velocity dispersion in galaxies is challenging, requiring spectroscopic observation across the full stellar disk. This has only been possible until recently, with the advent of Integral Field Unit (IFU) spectroscopic observations. The IFU-based surveys, e.g., ATLAS3D ([Cappellari](#)

et al., 2011), the Calar Alto Legacy Integral Field Area (CALIFA) survey (Sánchez et al., 2012; Walcher et al., 2014), the Mapping Nearby Galaxies at APO (MaNGA) survey (Bundy et al., 2014), the Sydney-Australian-Astronomical-Observatory Multi-Object Integral-Field (SAMI) survey (Croom et al., 2021) etc., have opened the opportunity to estimate the velocity dispersion in the stellar disk. These surveys provide direct measurements of the stellar velocity dispersion and can be used to estimate the realistic three-dimensional density distribution by solving Poisson’s equations.

In this work, we use the IFU data of the galaxy NGC 551 from Data Release 3 (DR3) of the CALIFA integral field unit (IFU) survey (Sánchez et al., 2016b) and estimate the vertical velocity dispersion in its stellar disk. Assuming the stellar disk to be in vertical hydrostatic equilibrium under the force field of other gas disks and the dark matter halo, we self-consistently solve joint Poisson’s equations of hydrostatic equilibrium to obtain a three-dimensional density distribution of the stellar disk. Using this density distribution and the rotation curve (estimated using HI data), we built a dynamical model of the stellar disk in NGC 551. This dynamical model is then projected into the sky-plane with the observed inclination and convolved with the telescope point spread function to produce a model surface density map, which is equivalent to the observation. We then compare this map with the observed surface density map to investigate the existence of a multi-component stellar disk in NGC 551.

To investigate the three-dimensional structures of the stellar disks in general, we apply our formalism to NGC 551. For NGC 551, all the data required to build a dynamical model are available publicly. Furthermore, this galaxy has properties similar to the Milky Way. A body of research has been conducted on the Milky Way to resolve the issue of thin and thick stellar disks. For example, Gilmore & Reid (1983) studied the star counts in the Galaxy and found that the vertical distribution shows a break and is better fitted by two exponential components rather than one, indicating the existence of a two-component disk. Furthermore, several authors using Gaia astrometric data (Andrae et al., 2018; Gaia Collaboration et al., 2021a) estimated the age of thousands of stars (see, e.g., Pinsonneault et al., 2018; Miglio et al., 2021) in the disk of the Galaxy.

These data sets were further used to build machine learning models and predict the age of an even larger number of stars (Ness et al., 2016; Anders et al., 2018; Mackereth et al., 2019; Wu et al., 2019; Ciucă et al., 2021). They found distinct age distributions consistent with two different populations in thin and thick disks. Several spectroscopic observations in the solar neighborhood also show a bimodal distribution in the $[\alpha/\text{Fe}]$ abundance (Bensby & Feltzing, 2006; Reddy et al., 2006; Lee et al., 2011). All these studies strongly indicate the existence of a two-component stellar disk in the Milky Way.

We have chosen NGC 551 as a representative of the Milky Way for our study. Comparing the galaxy with the Milky Way, we find that the NGC 551 is classified as SBbc (de Vaucouleurs et al., 1991), where SB stands for spiral galaxy with a bar, and the subcategory is based on how open or tight the arms of the spiral are, whereas the Milky Way is classified as SBc (Hodge, 1983) in the Hubble classification. Looking at the radii of both galaxies side by side, we find the isophotal diameter of the Milky Way to be 26.8 ± 1.1 kpc (Goodwin et al., 1998) in optical B-band, and for NGC 551, at a distance of 72 Mpc it is 38.11 ± 3.66 kpc (de Vaucouleurs et al., 1991) in optical B-band. The star formation rate (SFR) for the Milky Way was found to be $2.0 \pm 0.7 M_{\odot} \text{ yr}^{-1}$ (Elia et al., 2022), whereas the same for NGC 551 was measured to be $2.04 \pm 0.33 M_{\odot} \text{ yr}^{-1}$ (Bolatto et al., 2017). These SFR match each other very closely. The bolometric luminosity of these two galaxies is measured to be $(2.0 \times 10^{10}) L_{\odot}$ (van den Bergh, 1999) in V-band, and $(2.24 \times 10^{10}) L_{\odot}$ (Springob et al., 2007) in I-band, respectively.

Our study makes use of the IFU observation carried out by the CALIFA survey (Sánchez et al., 2012). The CALIFA survey has two observing modes: V500 and V1200, referring to low and medium spectral resolutions, respectively. The low-resolution V500 observations spanned the wavelength range from 3745 to 7300 angstroms with a spectral resolution (R) of ~ 850 at 5000 angstroms. Conversely, the medium-resolution V1200 observations covered the wavelength range from 3400 to 4750 angstroms with a higher spectral resolution (R) of ~ 1650 at 4500 angstroms. From the CALIFA survey, we constrain the number of galaxies for our study based on the parameters we require, as mentioned above.

For the stellar surface density (Σ_*), we require $3.6 \mu\text{m}$ wavelength observation. Initially, many CALIFA galaxies have been observed by the Spitzer Infrared telescope at $3.6 \mu\text{m}$ wavelength (Meidt et al., 2013), which helps us estimate stellar masses significantly more accurately than at other wavelengths. For the molecular gas surface density (Σ_{H_2}), the data are obtained from another survey called the EDGE-CALIFA survey (Bolatto et al., 2017). It uses an interferometric CO observation technique with the Combined Array for Research in Millimeter-wave Astronomy (CARMA) interferometer. The survey includes high-quality CO data for 126 galaxies, which is the largest interferometric CO survey of nearby galaxies. Furthermore, in our study, we also use IFU to measure stellar velocity dispersion σ_* . The IFU has a limited field of view. Hence, the total optical disk of a galaxy with large diameter at nearby distance might not get covered fully by IFU. However, to estimate accurate σ_* , the IFU coverage is essential. Furthermore, our modeling also requires HI observation of galaxies for kinematic information. As HI line is a forbidden line, it cannot be observed if the galaxy redshift is too high (the farthest redshift to which HI is detected in emission is 1.3 Chakraborty & Roy (2024)). Given these constraints, NGC 551 serves as one of the candidate galaxies, for which all the data are available and the modeling could be performed. Hence, we use NGC 551 for this study.

In Table 1.1, we mention the basic properties of this galaxy. The basic parameters are obtained from Skrutskie et al. (2006). The distance of the galaxy is calculated from the luminosity distance in Bolatto et al. (2017) using a Hubble constant of $69 \text{ km s}^{-1} \text{ Mpc}^{-1}$ (Freedman, 2021). The inclination is calculated by using MGEfit to the surface density distribution of Spitzer $3.6 \mu\text{m}$ data (this work).

Table 1.1: Basic properties of NGC 551.

Parameters	Values
RA ^a	01 27 40.66 (<i>h m s</i>)
Dec ^a	+ 37 10 58.5 (° ' ")
Inc ^b	63°
Dist ^c	72 Mpc
PA ^b	135°
SFR ^d	$2.04 \pm 0.33 \text{ M}_{\odot} \text{ yr}^{-1}$
Optical Diameter ^e (D_{25})	$109 \pm 10.5''$
Classification ^f	SBbc

^a Obtained from the two Micron All Sky Survey (2MASS) ([Skrutskie et al., 2006](#))

^b Obtained from the MGEfit of the galaxy

^c The distance calculated from the luminosity distance obtained from [Bolatto et al. \(2017\)](#)

^d ([Bolatto et al., 2017](#))

^e 25th B-magnitude isophotal diameter from HyperLEDA ([de Vaucouleurs et al., 1991](#); [Makarov et al., 2014](#))

^f ([de Vaucouleurs et al., 1991](#))



Figure 1.1: NGC 551
observed in R-band

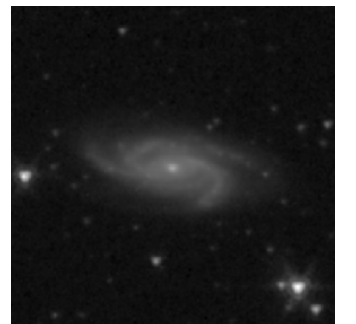


Figure 1.2: NGC 551
observed in 3.6 μm

Chapter 2

Hydrostatic Equilibrium

Hydrostatic equilibrium refers to the balance between the gravitational forces exerted by the mass distribution within the galaxy and the opposing pressure gradient arising from the motion of gas and stars.

The mathematical expression for hydrostatic equilibrium is given by:

$$\nabla P = -\rho \times \nabla \Phi,$$

where P is the pressure, ρ is the mass density, and Φ is the gravitational potential. This equation states that the gradient of the pressure must be equal and opposite to the gravitational force, ensuring that the net force on an infinitesimal volume element is zero.

Hydrostatic equilibrium is a crucial assumption in many astrophysical models because it allows for the determination of mass distributions, density profiles, and other properties of galaxies based on observable quantities, such as the rotation curves or velocity dispersion profiles. For hydrostatic equilibrium to be valid in galaxies, the following conditions need to be satisfied:

1. **Sufficient Random Motions:** In regions where the motions of stars or gas particles are predominantly random, with no significant bulk or organized flows, the pressure gradient arising from these random motions can balance the gravitational force. This condition is typically met in the galactic disk. In the vertical direction, the motions of the gas and stars are random, and they can be treated as a fluid and can establish vertical hydrostatic equilibrium.

2. In the galactic disk, the gravitational force exerted by the total mass distribution of the galaxy is the primary force acting on the gas particles. The thermal motions of the hot gas provide the necessary pressure gradient to balance this gravitational force, establishing hydrostatic equilibrium.

However, there are regions of the galaxy where the hydrostatic equilibrium might not be valid:

1. **Dynamically Perturbed Regions:** In regions of galaxies undergoing significant dynamical perturbations, such as mergers, tidal interactions, or strong outflows, the assumption of hydrostatic equilibrium may break down. These processes can introduce non-gravitational forces, turbulence, and complex motions that violate the assumptions of hydrostatic equilibrium.
2. **Cold Gas and Star-forming Regions:** In regions of active star formation, cold molecular gas clouds, and the associated stellar feedback processes can introduce complex dynamics and non-gravitational forces that may violate the hydrostatic equilibrium assumption. These regions often exhibit supersonic turbulence, outflows, and other phenomena that cannot be described by a simple balance between pressure gradient and gravitational forces. However, the fractional volume of such regions is limited and may not dominate the galaxy disk.
3. **Galaxies with Significant Non-thermal Pressure Components:** In some galaxies, particularly those hosting active galactic nuclei (AGN) or strong stellar winds, non-thermal pressure components, such as cosmic rays or magnetic fields, can contribute significantly to the total pressure. In these cases, the assumption of hydrostatic equilibrium based solely on thermal pressure may not be valid, and more complex models are required to account for the additional pressure components. However, these effects can only perturb a fraction of the disk volume in galaxies. In normal galaxies, the overall effect of these processes is expected to be marginal. Hence, the galactic disk in normal galaxies can be considered to be in vertical hydrostatic equilibrium. Thus, the stability and structure of these disks can be described by the equations of hydrostatic equilibrium.

2.1 Equation of Hydrostatic Equilibrium

We assume the galactic disk to be a collection of co-planar, axisymmetric, and concentric stellar, atomic, and molecular disks embedded within a dark matter halo. We also assume that these disks are in vertical hydrostatic equilibrium. These assumptions allow us to express Poisson's equation, which governs hydrostatic equilibrium, in cylindrical polar coordinates for any specific radial position within the disk as follows:

$$\frac{1}{R} \frac{\partial}{\partial R} \left(R \frac{\partial \Phi_{\text{tot}}}{\partial R} \right) + \frac{\partial^2 \Phi_{\text{tot}}}{\partial z^2} = 4\pi G \left(\sum_{i=1}^{n=3} \rho_i + \rho_{\text{dm}} \right). \quad (2.1)$$

In this equation, the total potential, denoted by Φ_{tot} , encompasses the combined gravitational effects of both the dark matter halo and the galaxy's baryonic disks (stars, atomic gas, and molecular gas). The volume density is represented by the variable ρ_i pertaining to distinct components within the disk system, with the index $i = 1, 2$, and 3 representing stars, atomic gas, and molecular gas, respectively. Additionally, ρ_{dm} represents the density associated with the dark matter halo. In a condition of vertical equilibrium, there is an equilibrium between the potential gradient along the perpendicular direction and the pressure gradient. This fundamental principle can be expressed through the Jeans equation.

$$\frac{\partial}{\partial z} \left(\rho_i \langle \sigma_z^2 \rangle_i \right) + \rho_i \frac{\partial \Phi_{\text{tot}}}{\partial z} = 0. \quad (2.2)$$

The symbol σ_z denotes the velocity dispersion associated with the various baryonic disks, serves as an indicator of the vertical pressure within the system. The velocity dispersion is assumed to be constant in the z -direction and to change only in the radial direction. By utilizing Eq. 2.2, we can simplify Eq. 2.1 in the following manner:

$$\begin{aligned} \langle \sigma_z^2 \rangle_i \frac{\partial}{\partial z} \left(\frac{1}{\rho_i} \frac{\partial \rho_i}{\partial z} \right) = & -4\pi G \left(\rho_s + \rho_{\text{HI}} + \rho_{\text{H}_2} + \rho_{\text{dm}} \right) \\ & + \frac{1}{R} \frac{\partial}{\partial R} \left(R \frac{\partial \Phi_{\text{tot}}}{\partial R} \right), \end{aligned} \quad (2.3)$$

The final term on the right side of Eq. 2.3 can be estimated using the knowledge of the rotation curve. This term arises from the radial gradient of the total

potential. To approximate this gradient, we can utilize the observed rotation curve, which serves as an indicator of the galaxy's potential within the mid-plane. As a result, the radial component can be approximated by the following equation:

$$\left(R \frac{\partial \Phi_{\text{tot}}}{\partial R}\right)_{R,z} = (v_{\text{rot}}^2)_{R,z}. \quad (2.4)$$

Here, v_{rot} represents the galaxy's rotation curve. Although Eq. 2.4 is rigorously valid only at $z = 0$, we operate under the assumption that the rotation curve remains relatively consistent across varying z -values and effectively represents the gravitational potential above $z = 0$. Taking this assumption into account, we can simplify Eq. 2.3 further by utilizing Eq. 2.4, resulting in the following form of the hydrostatic equilibrium equation.

$$\begin{aligned} \langle \sigma_z^2 \rangle_i \frac{\partial}{\partial z} \left(\frac{1}{\rho_i} \frac{\partial \rho_i}{\partial z} \right) = & -4\pi G \left(\rho_s + \rho_{\text{HI}} + \rho_{\text{H}_2} + \rho_{\text{dm}} \right) \\ & + \frac{1}{R} \frac{\partial}{\partial R} \left(v_{\text{rot}}^2 \right). \end{aligned} \quad (2.5)$$

Solving Eq. 2.5 at different radii will give us the volume density as a function of radius and height for all three disks. Thus, we obtain a complete three-dimensional density distribution of each disk.

2.2 Input Parameters to the Differential Equation

2.2.1 Surface Densities

We employ infrared data to compute the stellar surface density profile (Σ_*) rather than other SDSS visual bands like r and g. Infrared waves can pass through dust-obscured regions of the galaxy during observing, unlike SDSS bands, which are absorbed and scattered. Also, the majority of the galaxy's mass comes from the old stars, and the $3.6\ \mu\text{m}$ is better suited for studying cooler old stars. The infrared flux in the units of Mjy/str is converted into $\text{M}_\odot/\text{pc}^2$ using the calibration relation given by [Eskew et al. \(2012\)](#).

To estimate the surface density profile, the isophotes are fitted to the galaxy intensity distribution. This fitting technique gives good results when the brightness distribution does not deviate from an elliptical shape. However, in a spiral galaxy, the disk consists of multiple components, such as a nucleus, bulge, ring, spiral arms, etc., or asymmetries. In such cases, it is better to model the surface brightness as the sum of multiple two-dimensional Gaussians. This method is called the Multi Gaussian Expansion (MGE) fit of the surface brightness, and it has been widely used in the literature to estimate the surface brightness profile of galaxies ([Monnet et al., 1992](#); [Emsellem et al., 1994](#); [Cappellari, 2002](#)). We use this method to estimate the surface density profile of the stellar disk in NGC 551.

The MGE method first finds the galaxy's center and fits a Gaussian function to its brightness distribution. The projected surface brightness of the stellar disk can be represented as a sum of multiple Gaussians given as (see, e.g., [Cappellari, 2002](#))

$$\sum(R', \theta') = \sum_{j=1}^N \frac{L_j}{2\pi\sigma_j^2 q'_j} \exp \left[-\frac{1}{2\sigma_j^2} \left(x_j'^2 + \frac{y_j'^2}{q_j'^2} \right) \right], \quad (2.6)$$

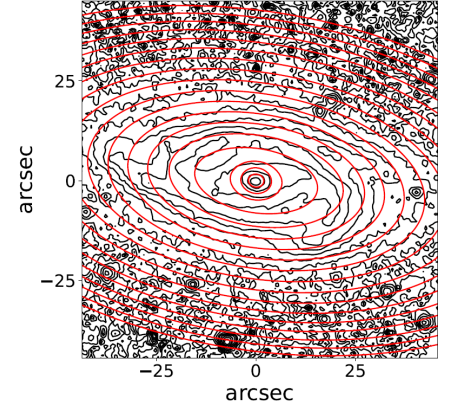
where (x', y', z') is a system of coordinates where the center is at the galaxy nucleus and the z' axis points towards the observer.

$$\begin{aligned} x'_j &= R' \sin(\theta' - \psi_j) \\ y'_j &= R' \cos(\theta' - \psi_j). \end{aligned}$$

Here, (R', θ') represent the polar coordinates within the plane of the sky (x', y') . Within this framework, N denotes the total number of Gaussian components employed, each characterized by its respective luminosity, L_j , the axial ratio ($0 \leq q'_j \leq 1$), dispersion, σ_j along the major axis, and position angle represented by ψ_j , which is computed by rotating the main axis clockwise relative to the y' axis.

The fit gives us the three parameters:

L_j , q'_j , and σ_j . The MGEfit method then subtracts the contribution of this Gaussian from the overall brightness and repeats with a slight offset to the initial position. After multiple iterations of this technique, the entire galaxy is fitted, and we obtain a table of all the Gaussian parameters.



In Fig. 2.1, we show the result of the MGE fit of the stellar disk of NGC 551, and in Table 2.1, the first column is the central surface density of the Gaussian. These Gaussian components are then appropriately

Figure 2.1: The MGE fit of NGC 551. The black contours represent the observed stellar surface brightness distribution, whereas the MGE-fitted contours to the isophotes are shown in red.

deprojected, incorporating the intrinsic

axial ratio of the disk, to construct the deprojected surface density profile. We show the deprojected stellar surface density profile in Fig. 2.3.

To calculate the 1σ uncertainties, we performed a Monte Carlo analysis by running MGEfit 100 times on surface density maps created by adding different realizations of noise. We add Poisson and Read noise appropriately with observed counts in each realization. This map is then used in MGEfit for surface density decomposition. We take the standard deviation of these Monte Carlo runs as the error. This error is then propagated through the deprojection process to obtain error estimates on the final surface density profile.

For the molecular surface density profile (Σ_{H_2}), we have used the moment

Σ_{\star}	σ	q'
$M_{\odot}\text{pc}^{-2}$	(pix)	
(1)	(2)	(3)
5806.02 ± 42.42	2.43	0.4307 ± 0.0023
497.88 ± 15.25	25.73 ± 0.18	0.4307 ± 0.002
73.44 ± 2.01	54.23 ± 0.05	0.4307 ± 0.0097

Table 2.1: MGEfit parameter of NGC 551

maps from the EDGE-CALIFA survey (Bolatto et al., 2017). Bolatto et al. (2017) used the Combined Array for Millimeter-wave Astronomy (CARMA) (Bock et al., 2006) interferometer to map molecular gas (CO ($J = 1 - 0$)) in 126 nearby galaxies as part of the survey. We use the total intensity map from the survey and convert the surface density to the unit of $M_{\odot} \text{pc}^{-2}$ from given flux in $\text{Jy km Bm}^{-1} \text{s}^{-1}$ by using the formula given in Bolatto et al. (2017).

$$M_{mol} = 1.05 * 10^4 \frac{S_{CO} \delta \nu D_L^2}{1 + z}. \quad (2.7)$$

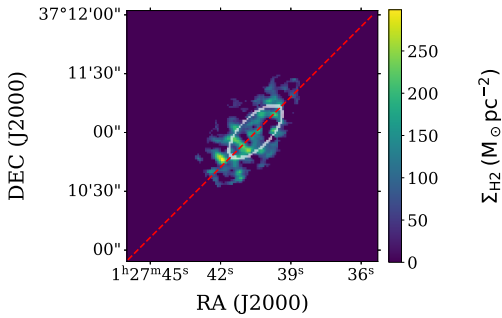


Figure 2.2: The Σ_{H_2} distribution in NGC 551. The white ellipse shows a representative annular region (a radial bin) at a radius of 6 kpc over which Σ_{H_2} was averaged to obtain a data point in the Σ_{H_2} profile. The red dashed line designates the major axis of the galaxy.

In this equation, $S_{CO} \delta \nu$ represents the integrated CO ($J = 1 - 0$) line flux measured in (Jy km s^{-1}), while D_L denotes the luminosity distance in megaparsecs (Mpc), and z stands for the redshift. It's important to note that this calculation assumes a CO-to- H_2 conversion factor of $X_{CO} = 2 \times 10^{20} \text{cm}^{-2} (\text{K km s}^{-1})^{-1}$, and it takes into consideration a factor of 1.36 to account for the mass adjustment due to helium. (Bolatto et al., 2013a).

To determine the radial profile of Σ_{H_2} , we make use of the position angle and the inclination of the

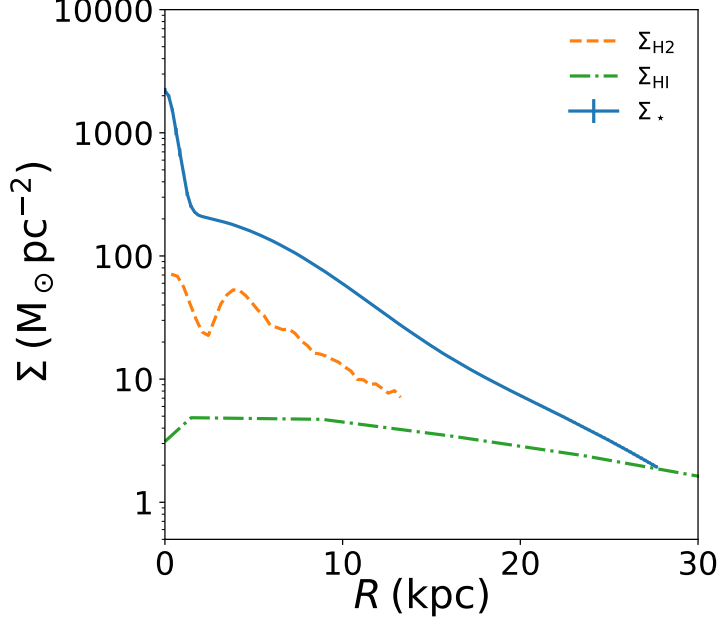


Figure 2.3: The deprojected surface density profiles of different disks in NGC 551. The solid blue line represents the stellar surface density, whereas the dashed orange and dashed-dotted green lines represent the molecular and atomic gas surface density profiles, respectively. Error bars reflect formal 1σ uncertainties in the stellar surface density.

molecular disk as given by [Bolatto et al. \(2017\)](#). We divide the disk into a series of concentric annular regions, each with a width equivalent to the telescope’s beam size ($4.8'' \times 3.79''$). We average the surface density values within each region to estimate an average surface density. In Fig. 2.2, we show one such annular region at a radius of 6 kpc. We note that the observed surface density is deprojected to calculate the face-on surface density. This resulting molecular surface density profile is shown in Fig. 2.3 as the orange dashed line.

Finally, for the atomic gas surface density Σ_{HI} , we have used the HI map obtained through the Giant Meterwave Radio Telescope (GMRT) ([Swarup et al., 1991](#)) observation (proposal code 39_037). The data were analyzed using the same technique described in [Biswas et al. \(2022\)](#) to obtain a HI spectrum cube. The next step involves fitting a 3D tilted ring model to this HI spectral cube using the Fully Automated TIRIFIC (FAT) ([Kamphuis et al., 2015](#)). The 3D tilted ring model is a common approach developed by [Rogstad et al. \(1974\)](#)

for extracting the kinematics of a galaxy, in which the galaxy is assumed to be made up of concentric tilted rings, with each ring having its own velocity, position angle, and inclination. When fitted, the surface brightness profile is obtained at different rings at various radii. This surface density profile is also corrected for the presence of Helium in the atomic gas disk. In Fig. 2.3, the green dashed-dotted line represents the surface density profile of the atomic gas disk in NGC 551.

In Fig. 2.3, we present the $\Sigma(r)$ profile for all three disks of our sample galaxy. As we can see, the Σ_* dominates among the three components for the entire radial range. Thus, the stellar disk is expected to primarily determine the vertical density distribution of the stars. In contrast, Σ_{H_2} has a shorter radial extent compared to the others. As we assume the baryonic disk in NGC 551 is a three component system (star + H I + H₂), our modeling requires Σ for each of the three components. Hence, we only solve for the hydrostatic equilibrium up to the last measured radius of, Σ_{H_2} which is 10.9 kpc.

2.2.2 Velocity Dispersion

The pressure gradient, which acts in opposition to the cumulative gravitational attraction exerted by all components, including the dark matter halo, within a given elemental volume, is predominantly influenced by the velocity dispersion. Hence, it is an important quantity in the hydrostatic equation. The pressure is calculated using the knowledge of the vertical velocity dispersion.

Before higher-resolution spectroscopy became available, earlier studies used an analytical formula to calculate the stellar velocity dispersion, which was used to solve the hydrostatic equilibrium equation. To calculate this, several assumptions were taken, like the stellar disk is assumed to be in hydrostatic equilibrium under solely its own gravity, and its scale height is said to be constant, with a flattening ratio of $\frac{l_{\star}}{h_{\star}} = 7.3 \pm 2.2$ (Kregel et al., 2002). Here, l_{\star} and h_{\star} are the scale length and scale height of the stellar disk, respectively. With these assumptions, the vertical velocity dispersion in the stellar disk can be given as $\sigma_{\star} = \sqrt{\frac{2\pi G l_{\star}}{7.3} \Sigma_{\star}}$ (Leroy et al., 2008; van der Kruit, 1988). This formula can then be further simplified as $\sigma_{\star} = 1.924 \sqrt{l_{\star} \Sigma_{\star}}$, where l_{\star} is in unit of kpc and Σ_{\star} is in unit of $M_{\odot} \text{ pc}^{-2}$.

However, these assumptions are often not fulfilled in galaxies and, thus, can lead to significant errors in the estimated vertical velocity dispersion. In many recent studies, it has been found that most galaxies exhibit flaring, i.e, their scale height increases with radius (Narayan & Jog, 2002; Banerjee & Jog, 2007; Robin et al., 2014; Mateu et al., 2012; Patra, 2020, 2019). Also, in these studies, only the stellar disk's gravity is taken into account (via Σ_{\star}) while determining the analytical formulation. Nevertheless, the system may receive a substantial amount of gravitational influence from the gas disks and the dark matter halo. In fact, this would significantly change how the σ_{\star} is estimated.

For these reasons, it is essential to determine the σ_{\star} directly through observation. We employ the IFU spectroscopic data from the CALIFA survey to calculate the stellar disk velocity dispersion. We employed the pyFIT3D pipeline (Lacerda et al., 2022), an enhanced iteration of the earlier Pipe3D pipeline (Sánchez et al., 2016a). Although both versions of the pipeline employ the same algorithm, the more recent version has been developed in Python, replacing the previous

implementation in Perl. We use the latest version to analyze the IFU data of NGC 551 from the CALIFA survey.

The pyPipe3D pipeline takes the IFU data and spatially bins it using the continuum segmentation binning (CS-binning) algorithm (Sánchez et al., 2016a). The spectra corresponding to the spaxels within each spatial bin are averaged and stored as a single spectrum, together with the average spatial coordinates. Thus, for each bin, we obtain a spectrum that corresponds to the mean of the individual spectra of all the spaxels within that spatial bin, with spectral pixels having bad values being masked. At the end of this process, the row-stacked spectra (RSS) are created. Each spectrum within the RSS file is analyzed using the pyFIT3D spectral fitting code, which separates the stellar continuum and the ionized emission spectrum from the observed spectral energy density at a single pixel. For this, first, the stellar kinematics and dust attenuation are estimated by generating model spectra using a simple set of Single Stellar Populations (SSPs) (Cid Fernandes et al., 2013). Next, the ionized gas emission line spectrum is obtained by subtracting the model spectra from the original data. This spectrum is then fitted with a few strong, well-known emission lines to obtain the emission line parameters. Next, by subtracting the emission line spectrum from the observed spectrum, we obtain a gas-free spectrum on which stellar population analysis is performed, where the spectrum is decomposed into a larger set of SSPs to obtain different properties, such as stellar age and metallicity. In the end, we obtain the final cube, from which we obtain the stellar velocity dispersion map (see, e.g., Lacerda et al., 2022, for more details).

We use the second moment map to estimate the stellar velocity dispersion. Using a similar approach to what we used to estimate the Σ_{H_2} profile, we extract a radial profile of the velocity dispersion by averaging σ_* values in elliptical annuli at different radii. In Fig. 2.4, we show one such annulus (white ellipse) at a radius of 6 kpc.

It's crucial to note that the profile depicts the intensity-weighted σ_* measured along the line of sight rather than the intrinsic velocity dispersion. The profile may diverge significantly from the true σ_* when galaxies exhibit significant beam-smearing effects on the stellar spectra along the line of sight, especially

in the central region of the galaxy where the rotation curve gradient is high. Three main factors lead to the blending of rotational velocity into the stellar spectral width: the orientation of the stellar disk, the slope of the rotation curve, and the spatial resolution. Due to these blending effects, the profile consistently provides an overestimated view of the intrinsic σ_* profile. We implement an iterative procedure, similar to the approach adopted in [Patra \(2020\)](#), to deduce the intrinsic σ_* profile from the observed MOM2 profile. More details on the technique can be found in subsection 2.2.5.

As radio interferometers allow for resolved spectroscopic observation of galaxies, determining the vertical velocity dispersion in the atomic and molecular disks is relatively straightforward. There have been extensive studies and analyses on the

HI velocity dispersion, σ_{HI} , in spiral galaxies using the HI spectral line studies. Early research has suggested that the σ_{HI} values range from 6 – 13 km s^{-1} , ([Shostak & van der Kruit, 1984](#); [Kamphuis & Sancisi, 1993](#)). A recent high-spatial-resolution study of 12 nearby galaxies found a $\sigma_{\text{HI}} = 11.9 \pm 3.1 \text{ km s}^{-1}$ ([Caldú-Primo et al., 2013](#)). However, work by [Mogotsi et al. \(2016\)](#) on the same sample found the σ_{HI} to be $11.7 \pm 2.3 \text{ km s}^{-1}$. Based on these investigations, we assume the σ_{HI} in spiral galaxies to be 12 km s^{-1} and solve the hydrostatic equilibrium equation.

Many studies have been undertaken to estimate the molecular velocity dispersion in the Milky Way and external galaxies. In earlier investigations conducted by [Stark \(1984\)](#), molecular clouds of different masses within our Milky Way were examined. Their findings revealed that low-mass molecular clouds with

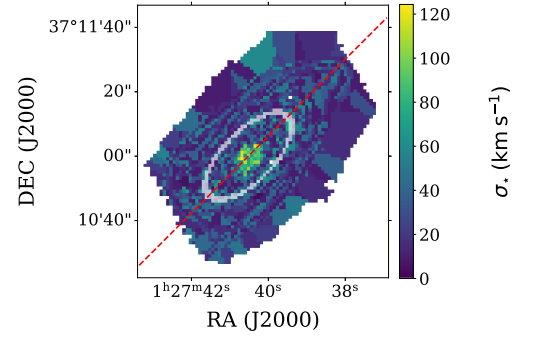


Figure 2.4: Stellar velocity dispersion map of NGC 551 from the third data release of the CALIFA survey. A velocity dispersion profile is generated by averaging velocity dispersion values in annular rings at different radial bins. The white elliptical region shows one such bin at 6 kpc. The red dashed line designates the major axis of the galaxy.

$10^2 M_{\odot} \leq M \leq 10^4 M_{\odot}$ exhibited a higher $\sigma_{H_2} \sim 9.0 \pm 1.0 \text{ km s}^{-1}$, whereas high-mass molecular clouds with $10^4 M_{\odot} \leq M \leq 10^{5.5} M_{\odot}$ displayed a lower $\sigma_{H_2} \sim 6.6 \pm 0.5 \text{ km s}^{-1}$. In a recent research conducted by [Marasco et al. \(2017\)](#), the molecular velocity dispersion inside the solar circle of the galaxy was found to be $\sim 4.4 \pm 1.2 \text{ km s}^{-1}$. In the study done by [Combes & Becquaert \(1997\)](#), the molecular gas velocity dispersion in two nearby spiral galaxies was found to be $\sim 6 \text{ km s}^{-1}$ and $\sim 8.5 \text{ km s}^{-1}$ respectively. This velocity dispersion was also found to be constant over the entire galaxy.

[Mogotsi et al. \(2016\)](#) looked into the velocity dispersion of the molecular disks in 12 nearby spiral galaxies. They found an average molecular velocity dispersion of $7.3 \pm 1.7 \text{ km s}^{-1}$. They also compared these velocity dispersion values with those in the atomic disks of the same galaxies. They found that the velocity dispersion in the atomic disk is almost two times higher than the average velocity dispersion in the molecular disk. Based on their findings, we adopt values of 6 and 12 km s^{-1} for velocity dispersion in the molecular and atomic disks, respectively. It is worth noting that our selection of these specific values has minimal impact on the calculated vertical density distribution within the stellar disk (see, e.g., [Patra, 2019](#); [Banerjee et al., 2011](#)). In the case of NGC 551, we varied the atomic and molecular velocity dispersion values within the allowed range of our adopted values. We found less than a 1% change in the scale height of the stellar disk due to this variation.

2.2.3 Rotation Curve

The rotation curve for NGC 551 is derived through the tilted ring fitting of the HI spectral cube. This technique is a standard method for performing kinematic modeling of galaxies (see, e.g., [Rogstad et al., 1974](#)). We have used the FAT ([Kamphuis et al., 2015](#)) pipeline to perform the fitting. This pipeline does not require any initial parameter guesses for fitting, unlike other kinematic modeling approaches, as it is automated. It takes the width of the ring to be fitted as the FWHM of the major axis of the beam by default, and the other parameters initial guesses are taken from the Source Finding Application (SOFIA [Serra et al. \(2015\)](#)). We feed the processed data cube (removing the emission-free

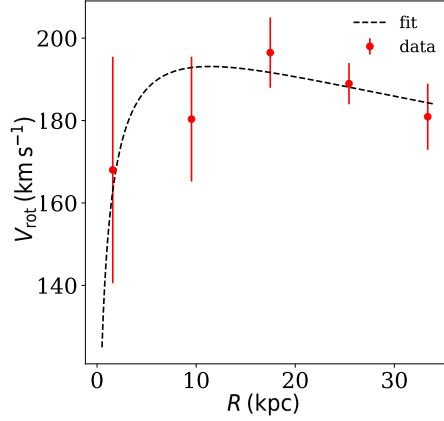


Figure 2.5: Rotation curve of NGC 551 derived from the HI spectral cube. The red circles with error bars represent the rotation curve, whereas the black dashed line signifies a fit to the rotation curve with a Brandt profile

Parameters	Values
Galaxy	NGC 551
V_{\max}	$193.1 \pm 3.98 \text{ (km s}^{-1}\text{)}$
R_{\max}	$11.4 \pm 2.6 \text{ kpc}$
n	$0.25 \pm .09$

Table 2.2: Brandt profile parameters from the fit

channels from the cube) to the pipeline, which gives us the rotation curve of the galaxy (see, e.g., [Biswas et al., 2022](#)). In Fig. 2.5, we plot the rotation curve.

In Eq. 2.5, we utilize the first derivative of the rotation curve. However, measurement limitations can introduce sharp variations in the rotation curve data, leading to unrealistic derivative values. To address this challenge, we fit the rotation curve to a Brandt profile ([Brandt, 1960](#)). Mathematically, the Brandt profile is expressed as:

$$V_{\text{rot}}(R) = \frac{V_{\max}(R/R_{\max})}{\left(1/3 + 2/3\left(\frac{R}{R_{\max}}\right)^n\right)^{\frac{3}{2n}}}. \quad (2.8)$$

In this equation, V_{rot} denotes the rotation velocity at any given radius, and V_{\max} represents the galaxy’s maximum rotation velocity, achieved at a radius of R_{\max} . The parameter n governs the rate of increase in the rotation curve as it approaches V_{\max} . The specific fitting parameters used for the galaxy rotation curve are provided in Table 2.2. By incorporating these parameters, we ensure that the resulting radial term is smooth and free from abrupt variations or deviations.

2.2.4 Dark Matter Halo Profile

The density of the dark matter halo, denoted as ρ_{dm} , plays a pivotal role in Eq. 2.5, where it counteracts the pressure exerted by the baryonic disks. We use the rotation curve of NGC 551, the stellar, HI, and molecular surface density profiles to build the mass model and to estimate the dark matter halo parameters.

Building upon the approach outlined by Biswas et al. (2023), we employ the stellar surface density profile derived from MGEfit. This profile is then used to calculate the stellar circular velocity using Jeans Anisotropic Modeling (JAM) (Cappellari, 2020). To achieve this, we assume a constant Mass-to-Light (M/L) ratio. For the gas component, the circular velocity is determined analytically based on the gas surface density, assuming a thin disk geometry. Finally, we decompose the observed total rotation velocity V_{rot} into contributions from stars, gas, and the dark matter halo. This decomposition is achieved by parametrically fitting the dark matter halo component.

$$V_{\text{rot}}^2 = V_{\star}^2 + V_{\text{HI}}^2 + V_{\text{H}_2}^2 + V_{\text{dm}}^2. \quad (2.9)$$

We fit the total velocity V_{rot} by using a Markov Chain Monte Carlo (MCMC) sampler (Fox, 1998) similar to the method described in Biswas et al. (2023). Previous investigations by Moore et al. (1998); Jing & Suto (2000) have suggested that the Navarro-Frenk-White (NFW) profile provides a more accurate representation of dark matter halos within spiral galaxies compared to an isothermal profile. Hence, we have chosen to employ an NFW distribution to describe the dark matter halo for NGC 551. The ρ_{dm} for an NFW distribution (Navarro et al., 1997) can be given as

$$\rho_{\text{dm}}(R) = \frac{\rho_0}{\frac{R}{R_s} \left(1 + \frac{R}{R_s}\right)^2}. \quad (2.10)$$

Here, ρ_0 represents the characteristic density, while R_s corresponds to the scale radius. These two parameters collectively are able to fully define a spherically symmetric Navarro-Frenk-White (NFW) dark matter halo.

The MCMC fit gives us two parameters: the concentration parameter, denoted as C , and M_{200} , which represents the average mass of the halo contained within a sphere where the density is 200 times the critical density of the Universe.

Following the estimation of the parameters C and M_{200} , we proceed to convert them into ρ_0 and R_s for use in Eq. 2.5. The relation between the C parameter and ρ_0 is established through the critical density ρ_c : From Eq. 2.10, the density at R_{200} is

$$\begin{aligned}\rho(R_{200}) &= \frac{\rho_0}{\frac{R_{200}}{R_s} \left(1 + \frac{R_{200}}{R_s}\right)^2} \\ &= \frac{\rho_0}{c(1+c)^2} = 200 * \rho_c.\end{aligned}$$

The critical density, ρ_c , is determined by assuming a value of zero for the cosmological constant Λ (as is the case for all standard Friedmann universes) and setting the normalized spatial curvature, represented as 'k,' equal to zero. When these substitutions are applied to the first of the Friedmann equations, as described by [Friedmann \(1999\)](#), we obtain:

$$\begin{aligned}\rho_c &= \frac{3H^2}{8\pi G} \\ &= 2.7754 * 10^{11} h^2 (\text{M}_\odot \text{ M pc}^{-3}),\end{aligned}\tag{2.11}$$

where $h = \frac{H_0}{100 (\text{km s}^{-1} \text{ Mpc}^{-1})}$. As NGC 551 is in the local universe, we have taken the value of H_0 to be $69 \text{ km s}^{-1} \text{ Mpc}^{-1}$ ([Freedman, 2021](#)). R_{200} is then related to the scale radius R_s as

$$R_{200} = CR_s.$$

The parameters M_{200} and R_s are connected via the concentration parameter C , as the total mass in the halo within R_{200} , which is given as:

$$\begin{aligned}M &= \int_0^{R_{200}} 4\pi r^2 \rho(r) dr \\ &= 4\pi \rho_0 R_s^3 \left[\ln(C+1) - \frac{C}{1+C} \right].\end{aligned}$$

Table 2.3: Dark Matter Halo Parameters

Parameters	Values
M_{200}	$5.43 \times 10^{11} (\text{M}_\odot)$
C	9.52
R_s	10.214 kpc
ρ_0	$28 \times 10^{-3} (\text{M}_\odot \text{ pc}^{-3})$

In Table 2.3, we present the dark matter halo parameters for NGC 551.

2.2.5 Solving the Hydrostatic Equation

Eq. 2.5 represents three coupled second-order partial differential equations, so we require two initial conditions to solve them, which can be given as,

$$(\rho_i)_{z=0} = \rho_{i,0} \quad \text{and} \quad \frac{d\rho_i}{dz} = 0. \quad (2.12)$$

As discussed in subsection 2.2.2, MOM2 is an overestimate of the intrinsic velocity dispersion obtained from the CALIFA IFU pipeline. Hence, using it directly in Eq. 2.5 would produce an incorrect three-dimensional density of the stars in the stellar disk. Therefore, we used a similar method to that used by Patra (2020), to iteratively solve for the densities as well as the intrinsic velocity dispersion σ_* .

In the first iteration, we start with the observed MOM2 profile as the intrinsic velocity dispersion and solve Eq. 2.5 to generate the stellar densities as a function of radius (R) and height (z). We build a 3D dynamical model of the stellar disk with this density distribution and the observed rotation curve. Next, we incline this 3D model to the observed inclination (63°), project it into the sky plane, and generate a spectral cube. This spectral cube is then convolved with the observed PSF of $2.28''$ ($\sim 796\text{pc}$), and collapsed to generate moment maps. The simulated MOM2 map is then used to construct a MOM2 profile, which is equivalent to an observation. In the first iteration, since we started with the MOM2 profile, which is already an overestimate of the σ_* , the simulated MOM2 would be higher than the observed one. In the next iteration, we adjust the observed MOM2 values (points outside the shaded region) by scaling them with a factor determined by the difference between these values and the σ_* from the previous iteration. We note that this multiplicative factor is different at different radii, ensuring faster convergence. In subsequent iterations, as the input MOM2 profile keeps getting lower, the simulated MOM2 approaches the observed one. We stop this method when the simulated and observed MOM2 values match within 5%. At this point, the input MOM2 can be considered the intrinsic σ_* , producing observed MOM2 self-consistently.

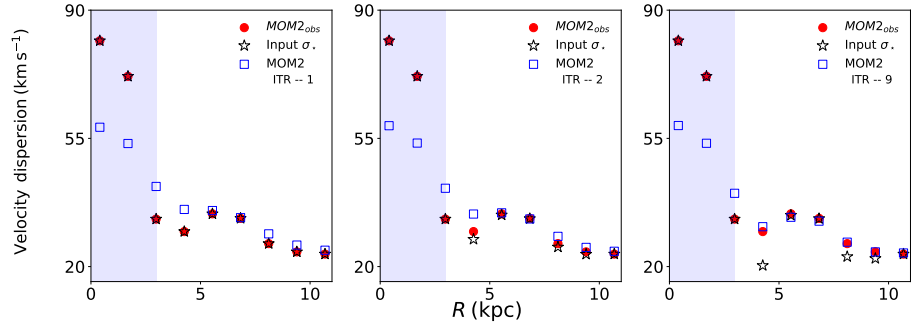


Figure 2.6: The iterative method workflow is illustrated. In each panel, the red circles represent the observed MOM2, the blue squares denote the simulated MOM2, whereas the black asterisks indicate the input intrinsic stellar velocity dispersion σ_* . The shaded region represents radii where we do not solve the iterative method. The left panel shows the results for the first iteration, whereas the middle and the right panel show the results for the second and ninth iteration. As can be seen, the iterative method for NGC 551 quickly converges within ten iterations. See the text for more details.

In Fig. 2.6, we show how our iterative method works. In the left panel, we show the first iteration, where the observed MOM2 is considered the input σ_* , resulting in a simulated MOM2 higher than the observed. In the subsequent iterations (middle and right panels), a lowered input σ_* results in simulated MOM2 profiles that are close to the observed ones. We obtain the intrinsic velocity dispersion from the method discussed above. This iterative method achieves convergence within 9 iterations.

Chapter 3

Results and Discussion

We note that the hydrostatic equilibrium condition is crucial to our formalism and the setting up of Eq. 2.5. However, this condition might be significantly violated in the central region of a star-forming galaxy. For example, there is evidence of elevated star formation (Irwin & Sofue, 1996; Bolatto et al., 2013b) in the central regions of galaxies. Recent studies by López-Cobá et al. (2019, 2020) on the potential effect of central outflow in the nearby universe found that these processes are not very frequent and that no single indication of outflow was found for NGC 551. Further, various factors, such as the steep gradient in the rotation curve and strong non-circular motions, can significantly broaden the stellar spectra in these regions. This artificial broadening can dominate the spectral width, particularly in galaxies with high inclinations, compared to the actual value of σ_* . Consequently, the effective MOM2 can become insensitive to intrinsic σ_* , causing the iterative method to diverge. To avoid these complications, we exclude the central region of NGC 551 from our modeling. We do not solve Eq. 2.5 at radii $R < 2$ kpc. Further, the molecular disk in NGC 551 extends to $R \sim 11$ kpc. Hence, we solve Eq. 2.5 between radii $2 \leq R \leq 11$ kpc at every 100 pc. The spatial resolution of the IFU data is ~ 796 pc at the galaxy distance of 72 Mpc. Hence, solving Eq. 2.5 every 100 pc is adequate for building the dynamical model. However, in the vertical direction, the effective resolution of the simulation (or solutions) is always maintained at better than 5 pc (see, e.g., Patra, 2020, for more details).

3.1 σ_* Profile

In almost all previous studies of hydrostatic modeling (Jog & Narayan, 2001; Patra, 2019, 2021), the stellar velocity dispersion was calculated analytically. However, there are several shortcomings in the assumptions of this calculation. For example, the stellar disk is considered to be in hydrostatic equilibrium under its own weight. The scale height of the stellar disk is considered to be constant at all radii, and it is related to the scale length by a constant flattening ratio $l_*/h_* = 7.3$. These assumptions do not apply in general. The scale height does not remain constant as a function of radius (López-Corredoira et al., 2002; Yusifov, 2004; Momany et al., 2006; Feast et al., 2014; Kalberla et al., 2014; López-Corredoira & Molgó, 2014), and the flattening ratio can vary considerably from galaxy to galaxy (Bizyaev et al., 2014; De Geyter et al., 2014; Peters et al., 2017; Reshetnikov et al., 2019).

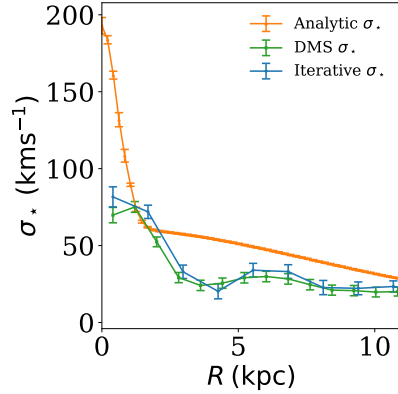


Figure 3.1: The velocity dispersion profiles of the stellar disk in NGC 551. The orange triangles represent the σ_* as obtained by analytical calculation from Leroy et al. (2008). The blue circles show the σ_* profile as obtained by the iterative method. The green squares show the σ_* profile obtained by the Disk Mass Survey (Bershady et al., 2010b). Error bars reflect formal 1σ uncertainties in the velocity dispersion.

The total gravity in the system can have considerable contributions from the gas and the dark matter halo. Thus, the actual velocity dispersion can be very different from that calculated analytically.

In Fig. 3.1, we plot the stellar velocity dispersion in NGC 551 as obtained by the iterative method (blue circles) along with that calculated analytically (orange triangles). As can be seen, the σ_* values are considerably different. For NGC 551, the intrinsic σ_* can differ from the analytical value by as much as 70%. This, in turn, can change the stellar scale height by a factor of 1.5 – 2.0. Hence, the analytical estimation of the vertical velocity dispersion in the

stellar disks might often overestimate the thickness of the disks. In the literature, other methods are also used to estimate the stellar velocity dispersion. For example, the Disk Mass Survey (DMS) has observed 46 face-on galaxies through CALIFA IFU, for which they have obtained stellar velocities and velocity dispersions. They obtained the line-of-sight stellar velocity dispersion, which is a projection along the line-of-sight of the stellar velocity ellipsoid (SVE). Using the principal SVE ratios, they obtained a relation between the projected velocity dispersion and the deprojected velocity dispersion (see, e.g., [Bershady et al., 2010a](#), for more details). Using the observed principal SVE ratios, the stellar velocity dispersion in NGC 551 can be calculated. In Fig. 3.1 the green squares represent the thus estimated σ_* . As can be seen, the DMS σ_* matches the σ_* obtained by the iterative method reasonably well (better than that calculated analytically). However, it should be noted that the DMS samples are mostly face-on galaxies, and their method is suitable for low-inclination galaxies ranging from 25° to 35° compared to our galaxy with 63° inclination.

To calculate the error bars, first, we obtain the error map of the velocity dispersion, provided as a PIPE3D output, while performing CALIFA data analysis. We extracted a radial profile of the velocity dispersion error by averaging the values in elliptical annuli at different radii. This error was then propagated to calculate uncertainties in the DMS velocity dispersion. For calculating the error on analytically calculated velocity dispersion, we use the formula $\sigma_* = 1.924\sqrt{l_*\Sigma_*}$ and propagate the error from Σ_* (calculated in Sect. 2.2.1).

To calculate the error bars on the velocity dispersion obtained in the iterative method, a rigorous error analysis would require propagating uncertainties from all parameters in Eq. 2.5. A Monte Carlo approach would be suitable, with bootstrapping multiple instances and running the iterative method. However, the iterative method is a computationally intensive method, and it takes ~ 4 hours per run on our workstation. This restricts us to using a Monte Carlo method to estimate the error in the velocity dispersion profile. Instead, we consider 1σ limits of the two most important input parameters, i.e., the stellar surface density and the observed velocity dispersion, to extract the limits of

the intrinsic velocity dispersion profile. We perform four runs of the iterative method by considering $\pm 1\sigma$ limits on stellar surface density and the observed velocity dispersion, and obtain the intrinsic velocity dispersion. The maximum difference of these profiles is then used in the standard error-propagation formula to obtain the final uncertainty. We note that, in principle, uncertainties on all the input parameters should be folded in to calculate the final uncertainty. However, as the contribution of other input parameters, as compared to the stellar surface density and stellar velocity dispersion, is insignificant, their contribution in determining the error bar is expected to be minimal.

3.2 Three-dimensional density distribution in the stellar disk

The solutions of the hydrostatic equation provide the volume densities of different disk components as a function of R and z . We solve this equation every 100 pc from a radius of 2 kpc to 11 kpc. Fig. 3.2 shows the density solutions (solid lines) for different disks in NGC 551 at a radius of 6 kpc. We also compare these solutions with those obtained using the stellar velocity dispersion calculated from the analytical expression (dashed lines). As shown in the figure, the analytically calculated σ_* produces lower densities at the midplane, and consequently, the disk extends to larger heights. This produces thicker stellar disks than expected. Further, as the other disks (atomic and molecular) are coupled to the stellar disk through gravity, they also become thicker than expected. For NGC 551, at a radius of 6 kpc, the midplane IFU computed and analytically calculated stellar, atomic, and molecular densities can differ by $\sim 91\%$, $\sim 25\%$, and $\sim 22\%$, respectively.

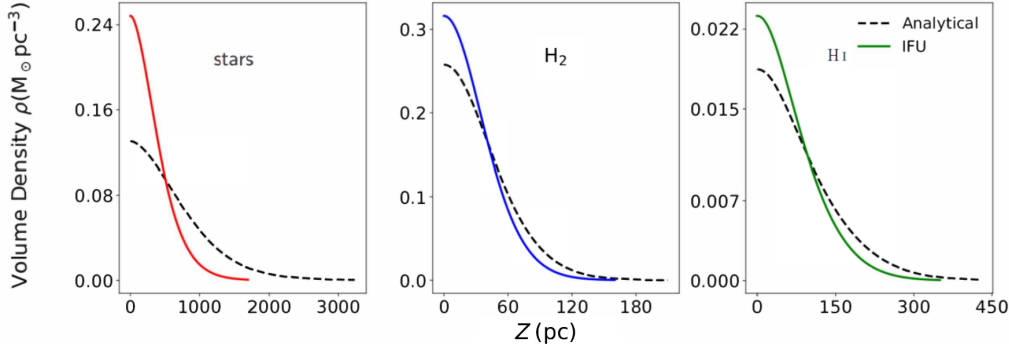


Figure 3.2: The solutions of the hydrostatic equilibrium equation at a radius of 6 kpc. The left, middle, and right panels present density solutions for stars, molecular, and atomic gas respectively. The solid lines in each panel represent solutions when the hydrostatic equations were solved with the iterative method using CALIFA IFU data. The dashed lines represent the solutions with the analytically calculated stellar velocity dispersion.

The half-width at half maximum (HWHM) is an excellent measure of the thickness of a baryonic disk. This HWHM is often adopted as the scale height of the density distribution in the vertical direction. Using our solutions, we estimate the scale height of different disk components as a function of radius.

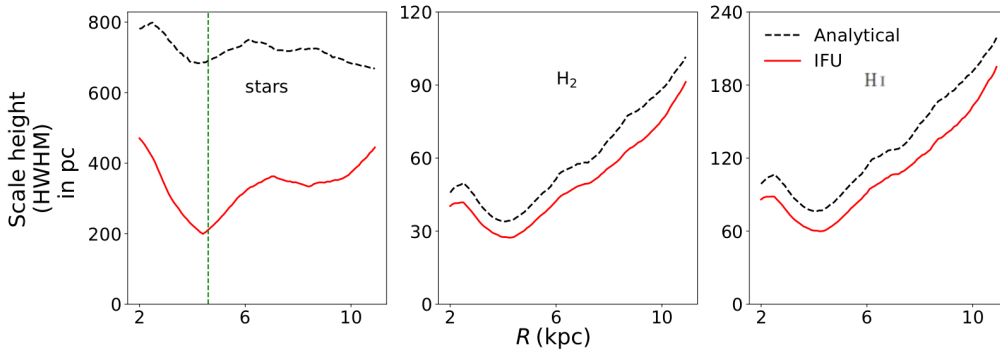


Figure 3.3: The scale height of different baryonic disks in NGC 551 under hydrostatic equilibrium. The left, middle, and right panels represent scale heights for the stellar, molecular, and atomic disks respectively. The solid lines in each panel represent the scale height due to our iterative method, whereas the dashed lines represent the same for our analytically calculated σ_* . The vertical dashed line in the left panel indicates the scale length of the stellar disk (4.6 kpc).

In Fig. 3.3, we plot the scale height of different disk components (solid lines) in NGC 551. We also compare the scale height profiles for solutions with analytically calculated σ_* , shown by dashed lines. As can be seen from the figure, the scale height of the stellar disk can be overestimated by up to a factor of two when using an analytically calculated σ_* . This difference is lower in the atomic and molecular disks; however, it can also make a difference of $\sim 25 - 30\%$. This indicates that the determination of the stellar velocity dispersion by the spectroscopic method is crucial for assessing the vertical density distribution in the baryonic disks (especially in the stellar disk) in galaxies. Next, we use the density solutions of the stellar disk and the observed rotation curve to build a three-dimensional dynamical model of NGC 551. We incline this dynamical model to the observed inclination of 63° , project it into the sky-plane, and construct a spectral cube. This cube is then convolved with the PSF of the IFU observation, and consequently, moment maps are made. These model moment maps are equivalent to an observation.

3.3 Two-component (thin+thick) stellar disk in NGC 551?

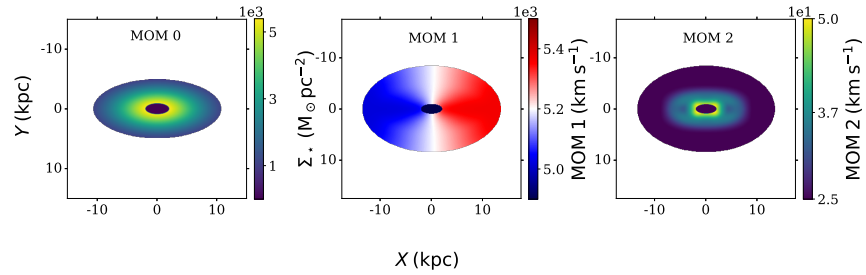


Figure 3.4: The simulated moment maps of the stellar disk in NGC 551. The left panel shows the moment zero map, i.e., the total surface brightness map in the units of $M_\odot \text{ pc}^{-2}$. The middle panel shows the moment one map or the velocity field of the galaxy. The right panel represents the velocity dispersion map. The last two maps have units of km s^{-1} . These moment maps are generated using the simulated spectral cube obtained through the dynamical modeling of the stellar disk.

In Fig. 3.4, we show our model moment maps of the stellar disk in NGC 551. We compare these mock maps with real observations to check the consistency of our modeling. To do so, we take vertical slices of the model and the observed surface density maps at different radii and compare the resulting profiles. In Fig. 3.5, we show representative vertical slices of the surface density map at radii of 2.5 kpc and 5.0 kpc. In Fig. 3.6, we show the resulting vertical surface brightness profiles at different radii. We take slices at radii of 2.5, 3.5, 4.5, and 5 kpc. We compare our model (blue lines) with surface density profiles from IFU maps (broken lines in top panels) as well as those from the $3.6\ \mu\text{m}$ maps (broken lines in bottom panels). As can be seen from the figure, the model profiles match the observations reasonably well. However, we note that at the central region (around $z \sim 0$ kpc), the observed map has an extra emission which is not seen in the simulated map. This emission looks like a distinct component with a sharp peak. This sharp peak is more prominent in the IFU map than in the $3.6\ \mu\text{m}$ map. Further, in both the top and bottom panels, it can be seen that as the radius increases, the amplitude of this peaked component decreases.

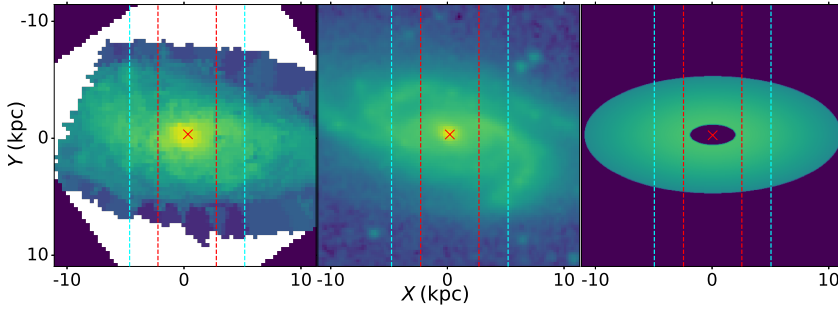


Figure 3.5: Vertical slices taken at different radii to compare the simulation with observation. The left panel represents the surface brightness map of the stellar disk as obtained by IFU observation. The middle panel shows the stellar disk as observed in Spitzer $3.6\ \mu\text{m}$ data. The right panel shows our simulated intensity distribution. The crosses in each panel indicate the center of the galaxy. The red and the cyan dashed lines denote the region ($2.5 - 5$ kpc) over which the simulation and the observations are compared.

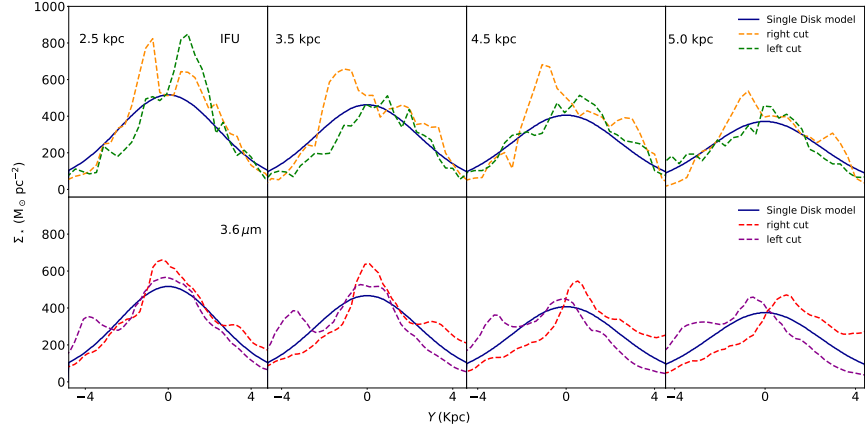


Figure 3.6: Comparison of vertical slices of the surface density distribution in the stellar disk of NGC 551. In the top panels, we compare the IFU observation with the simulation, whereas in the bottom panels, we compare Spitzer $3.6 \mu\text{m}$ with the simulation. The different panels represent comparisons at different radii. In each panel, the solid lines denote the simulated vertical slices profiles. Dashed lines show the observed vertical profiles. Two different colors represent two different halves (left and right) of the observed map. As can be seen from the figure, the simulated profiles at different radii match the observations very well, except at the central region.

This extra thin component could be a signature of a two-component disk in NGC 551. We have considered only one thick disk for hydrostatic modeling, for which the typical stellar velocity dispersion varies between 20-60 km/s (see Fig. 3.1). This, in turn, only produces the thick disk, which matches the vertical slices of the surface brightness profiles at larger heights (higher z values) but fails to produce a sharp feature at the center. Further, the amplitude of this sharp component is lower in the bottom panel ($3.6 \mu\text{m}$ map) compared to the top panels (IFU map). We know that $3.6 \mu\text{m}$ traces old stars (see, e.g., [Pahre et al., 2004](#); [Meidt et al., 2014](#); [Nidever et al., 2014](#)), whereas the wavelength range for the IFU observation is $3745 \text{ \AA} - 7500 \text{ \AA}$, which encompasses the optical band, which mostly traces young stars. This wavelength range mostly traces recent star formation, which is a classic signature of a thin disk. We further notice that the amplitude of this component decreases as a function of radius. At a radius of $\sim 5 \text{ kpc}$, the signature of this component is almost negligible. We

do not compare the vertical slices at radii larger than 5 kpc. At these radii, non-azimuthally asymmetric structures (e.g., the spiral arms) become prominent, hindering the direct comparison with our symmetric model.

3.4 Multi Component Models

As seen in Fig. 3.6, the vertical slices across the observation and the single thick disk model do not match each other in the central region. This extra emission could be due to the presence of a thin disk, a bar, or a combination of both. To test this, we constructed two new models: one with a thick and thin stellar disk model and one with a thick disk and bar. Using the same approach, we build 3D dynamical models for these new multi-structure models and produced moment maps. These maps were further used for comparison with observations.

3.4.1 Thick + Thin Model

Recent studies by [Snaith et al. \(2014\)](#); [Bland-Hawthorn & Gerhard \(2016\)](#); [Mosenkov et al. \(2021\)](#) have calculated the surface density ratio of thick disk and thin disk (f_{Σ}) from observations, making them able to estimate the mass percentages of thick and thin stellar disks in the Galaxy. Given the similarity between NGC 551 and the Milky Way, we have used this ratio to build our thick + thin model. In the study by [Mosenkov et al. \(2021\)](#), they discussed the structure of the Galaxy based on photometry from the WISE telescope at $3.4\mu\text{m}$ wavelength. In their study, they found a maximum and minimum value of, f_{Σ} which produce observables that matches best for the Milky Way. As both $3.4\mu\text{m}$ and $3.6\mu\text{m}$ are infrared wavelengths, we chose the f_{Σ} value from their study for our modeling as well. We built two models with values of $f_{\Sigma} = 0.38$ and 0.12 . With the value 0.38 , the mass composition in NGC 551 is 42% for thick disk and 58% for thin disk, and the surface density can be broken as 27.5% and 72.5% for thick and thin disk, respectively. Similarly, with a value 0.12 , we get 18% and 82%, respectively, for mass composition and 10.7% and 89.3%, respectively, for surface density.

There have also been extensive studies ([Lewis & Freeman, 1989](#); [Vieira](#)

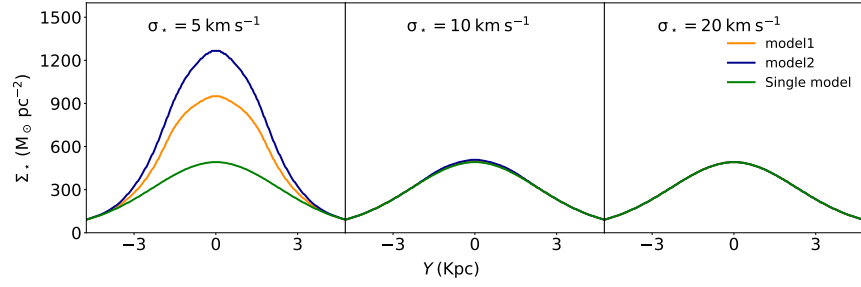


Figure 3.7: Comparing model 1 (27.5% Σ_* for thick disk), model 2 (10.3% Σ_* for thick disk) and single disk model MOM 0 map vertical slices Σ_* profile at a radius of 2.5 kpc. The green solid line represents the single disk model. The orange and blue solid lines represent the thick + thin model 1 and model 2 respectively.

et al., 2022) to determine the value of thin stellar disk velocity dispersion ($\sigma_{*,\text{tn}}$) in the Galaxy. Throughout the literature, different values have been found by different studies that use different techniques. A study by Lewis & Freeman (1989) found a value of 18 km s^{-1} around the solar neighborhood by observing 600 K giant stars with broadband photometry and medium resolution spectroscopy. A recent study by Vieira et al. (2022) found a value of $\sigma_{*,\text{tn}} = 31 \text{ km s}^{-1}$ by studying the kinematics of 296,879 RGB stars in the solar neighborhood. We also know that the thin, younger stellar disk velocity dispersion $\sigma_{*,\text{tn}}$ is found to be lower than the thick, older stellar disk velocity dispersion $\sigma_{*,\text{tk}}$ (Soubiran et al., 2003; Ivezić et al., 2008; Bensby et al., 2011; Robin et al., 2022). The $\sigma_{*,\text{tk}}$ for NGC 551 observed from CALIFA IFU is shown in Fig.3.1. The minimum value is $\sim 20 \text{ km s}^{-1}$, and hence, we did not use any value larger than it. As there is no observation of $\sigma_{*,\text{tn}}$ for NGC 551 due to the lack of resolution of current telescopes, we have varied the $\sigma_{*,\text{tn}}$ from 5 to 20 km s^{-1} to see which value matches with the observation slice profile.

This model now consists of four disk components, which are represented by four second-order coupled differential equations. Solving these equations with the same method as before for the single disk model is not possible, as the increase in system complexity can lead to numerical instability and convergence issues. The iterative approach that proved effective for three coupled equations was not able to converge due to the more intricate interactions and potential

stiffness in the four-equation system. Increased error accumulation, and the need for more sophisticated error estimation techniques further complicate the solution process.

To avoid this issue, we initially solved for the thick disk components using the established three-equation solver consisting of a stellar thick disk, an atomic gas disk, and a molecular gas disk. These components were solved simultaneously, allowing for their mutual gravitational interactions. After obtaining a stable solution for the thick components, we fixed these density distributions, and solved for the thin stellar disk. By treating the thick components as fixed, we effectively reduced the problem back to a single differential equation, with one that incorporates the gravitational effects of the previously solved thick components. This approach allowed us to maintain numerical stability while still capturing the essential physics of the four-component system. While this method does not solve all four equations simultaneously, it provides a physically reasonable approximation that balances computational feasibility with physical accuracy.

In Fig. 3.7, we show the vertical slices at a radius of 2.5 kpc across all three models. We observe that for a combined thick + thin model, as we reduce the $\sigma_{\star, \text{tn}}$, the peak of the profile starts to increase. In the rightmost panel, we have the model with $\sigma_{\star, \text{tn}} = 20 \text{ km s}^{-1}$, which is the same as $\sigma_{\star, \text{tk}}$ at the outer radius. Hence, we do not see any difference between the single thick model (green solid line) vertical slice and the thick + thin model (orange and blue solid line). As we move to the middle panel, with $\sigma_{\star, \text{tn}} = 10 \text{ km s}^{-1}$, we start to see small peaks compared to the single disk model, and at 5 km s^{-1} , the peak becomes much larger. By varying the $\sigma_{\star, \text{tn}}$, we found that model 1 ($f_{\Sigma} = 0.38$) vertical slices match the observation at $\sigma_{\star, \text{tn}} = 6 \text{ km s}^{-1}$, and for model 2 ($f_{\Sigma} = 0.12$) they match at 7 km s^{-1} . Further, comparing model 1 (72.5% Σ_{\star} for thin disk) and model 2 (89.3% Σ_{\star} for thin disk), we find that the model in which the thin disk comprises a higher surface density fraction of the galaxy shows a higher peak compared to the lower mass model with the same $\sigma_{\star, \text{tn}}$ as seen in the left and middle panels of Fig. 3.7. Next, we compared the MOM-2 radial profile of all models with observed IFU data, as shown in Fig. 3.8. From left to right panels,

we compare the model build with $\sigma_{*,\text{tn}} = 5, 10, \text{ and } 20 \text{ km s}^{-1}$, respectively. For all six combinations of models, the maximum difference between the MOM-2 radial profile and the observed IFU radial profile is 15%, which is around 4 km s^{-1} , and this is well within the observational uncertainties. Hence, just by looking at the MOM2 profiles, it is difficult to identify a particular model as explaining the observations best.

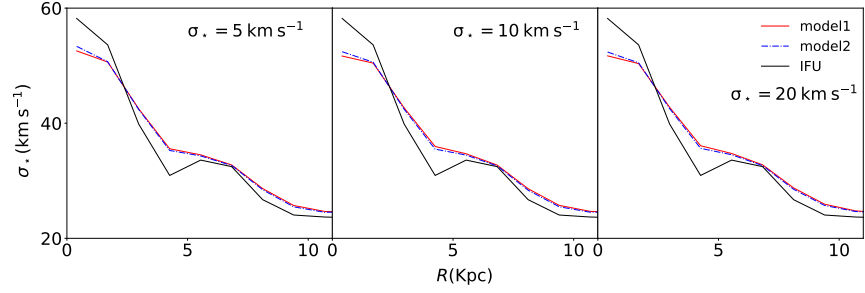


Figure 3.8: Comparing MOM-2 radial profiles for different models with different $\sigma_{*,\text{tn}}$. The black solid line represents the radial profile as obtained by the CALIFA IFU. The red and blue solid line represents the radial profile as obtained from the simulated MOM-2 maps of model 1 and model 2, respectively.

3.4.2 Thick + Bar Model

We further investigated whether the presence of a bar in NGC 551 can explain the observations. NGC 551 is classified as a barred spiral galaxy (SBbc). In a recent study by [Cuomo et al. \(2019\)](#), they found the strength of the bar and have categorized it as a weak bar. To incorporate the bar into the model, we fit a multi-component model consisting of a Sérsic profile, an exponential profile, and a second Sérsic profile. The Sérsic profile is used to fit the bulge region of a galaxy. The exponential profile is used to fit the disk region, and the second Sérsic profile is used to fit the bar region of a galaxy. For fitting, we used GALFIT software. The fit requires four files. The Spitzer $3.6 \mu\text{m}$ image, the PSF image, the noise file, and the mask file. The Sérsic profile is defined as

$$\Sigma_e \exp \left[-b_n \left[\left(\frac{r}{r_e} \right)^{\frac{1}{n}} - 1 \right] \right]. \quad (3.1)$$

Table 3.1: Best-fit parameters from the Sérsic + exponential disk + Sérsic model

Parameter	Bulge (Sérsic)	Disk (Exponential)	Bar (Sérsic)
x_c	118.85 ± 0.02	118.9 ± 0.06	118.21 ± 0.08
y_c	118.95 ± 0.02	119.98 ± 0.02	119.39 ± 0.02
m_{tot}	16.83 ± 0.01	13.18 ± 0.01	16.73 ± 0.01
r_e	1.59 ± 0.03	—	10.34 ± 0.15
r_s	—	23.09 ± 0.07	—
n	0.89 ± 0.09	—	0.36 ± 0.02
q	0.61 ± 0.02	0.43 ± 0.01	0.52 ± 0.01
PA	76.06 ± 1.82	85.46 ± 0.12	77.26 ± 1.53

It has 7 parameters to fit : $x_0, y_0, m_{\text{tot}}, r_e, n, e$, and PA . Here, x_0 and y_0 are the pixel co-ordinate of the galaxy. m_{tot} is the integrated magnitude of the galaxy. r_e is the effective (half-light) radius. e is the axis ratio, PA is the position angle, and n is the Sérsic index.

The exponential profile is defined as

$$\Sigma_0 \exp \left(-\frac{r}{h} \right). \quad (3.2)$$

It has 6 parameters to fit: $x_0, y_0, m_{\text{tot}}, h, e$, and PA . Here, h is the disk scale length.

Performing a multicomponent fit with these many parameters is time-consuming and prone to parameter degeneracy. To avoid this issue, we fit the components one by one. First, we fit only Sérsic profile. Keeping the geometric parameters (ellipticity and position angle) bounded in the value found in the first fit, we add the exponential disk. Again, keeping the geometric parameters of both Sérsic and exponential bounded, we added the second Sérsic profile. Table. 3.1 shows the multi-components fit.

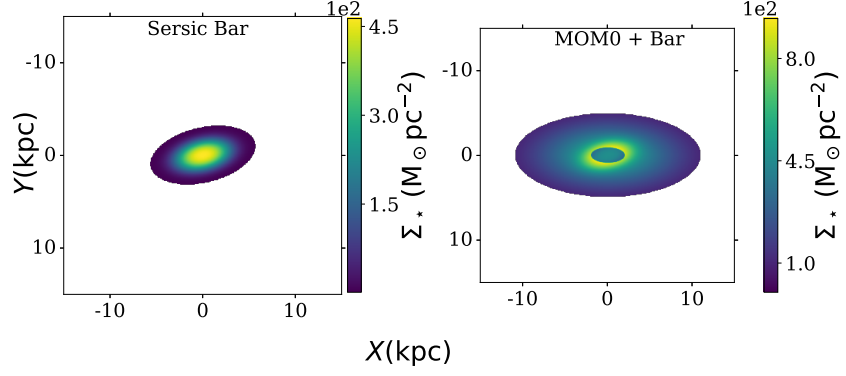


Figure 3.9: The left panel shows the 2D bar generated from the Sérsic bar profile. The right panel shows the MOM-0 map of thick disk + bar model of NGC 551.

Converting the bar parameters, we get the bar surface brightness = 0.84 ± 0.01 Mjy/str and the bar length = 2.16 ± 0.03 kpc. We obtained n and $e = 0.36 \pm 0.02$ and 0.52 ± 0.01 , respectively. These values are consistent with those expected for a weak bar in NGC 551, as also found by [Gadotti \(2008\)](#).

Finally, after getting the bar parameters, we added it into the projected MOM-0 map of our model (see Fig. 3.9). Next, we show the comparison of the vertical slices across the model and the observations in Fig. 3.10. Comparing, Fig. 3.6 and Fig. 3.10, we see the increase of the surface density in the slices due to the presence of bar much in the radial cut of 2.5 and 3.5 kpc. After adding the bar, the Spitzer map slices match the observations reasonably well. However, we note that at larger radii, such as 5 kpc, the bar model fails to produce the peak. Hence, it is possible that in NGC 551, a thin disk is required along with a bar to explain the observed surface density distribution.

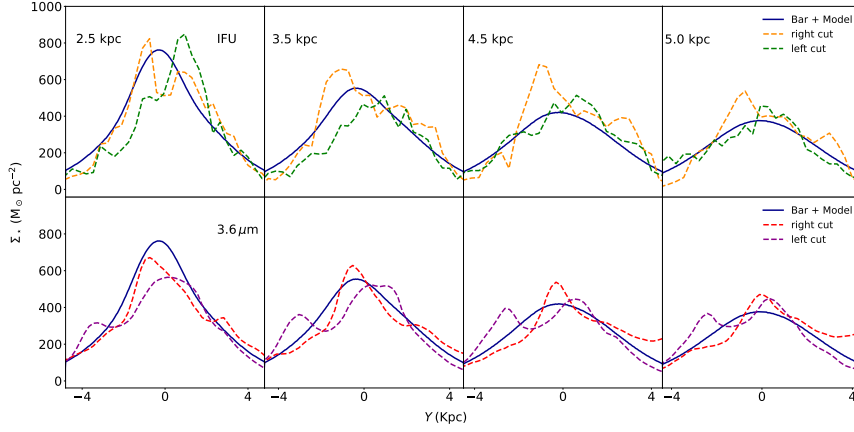


Figure 3.10: Comparison of vertical slices of the surface density distribution in the stellar disk of NGC 551. In the top panels, we compare the IFU observation with the bar+thick disk model, whereas in the bottom panels, we compare Spitzer $3.6 \mu\text{m}$ with the bar+thick disk model. The different panels represent comparisons at different radii. In each panel, the solid lines denote the simulated vertical slices profiles. Dashed lines show the observed vertical profiles. Two different colors represent two different halves (left and right) of the observed map.

3.5 Edge-On Models

Several studies have focused on stellar surface density distributions of the edge-on galaxies to investigate multi-component stellar disks (Yoachim & Dalcanton, 2006; Comerón et al., 2011b) in external galaxies. These studies find that the observed stellar surface density is better described by a two-component stellar disk. However, the observed surface density for an edge-on disk is the sum of all the light along a sight-line from different radii. Further, as the scale height of the stellar disk changes as a function of radius (for both the thin and the thick disk), the integrated light might not reflect the true nature of the disk.

To test this, we incline our 3D dynamical model to an inclination of 90° and project it to the sky plane to produce an edge-on surface brightness map. This is equivalent to how we would see NGC 551 in an edge-on orientation. We then use this map as a template to investigate if the traditional methods of fitting multi-component stellar disks to the edge-on surface brightness distribution can

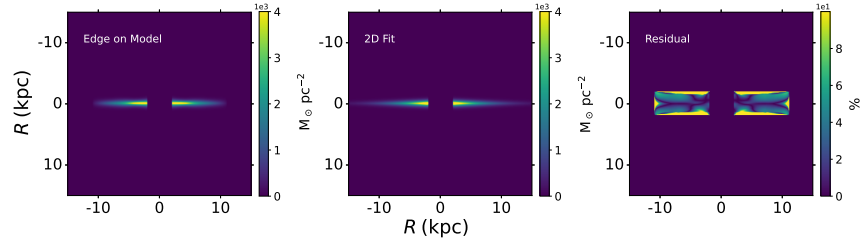


Figure 3.11: The surface brightness map of the stellar disk in NGC 551 in an edge-on orientation. The left panel shows the surface brightness map, whereas the middle panel represents a 2D fit to the map with the modified Bessel Function of the first kind $K(x)$ and a sech^2 . The right panel shows the residual of the fitting. The blanked portion in the middle of each panel represents the region where we do not solve the hydrostatic equilibrium equation.

recover the original disk parameters.

To do so, we have taken a widely used approach and fitted the 2D surface brightness distribution with modified Bessel functions of the first kind $K(x)$ and a sech^2 as done in [van der Kruit & Searle \(1981\)](#); [Yoachim & Dalcanton \(2006\)](#); [Comerón et al. \(2011a\)](#); [Mosenkov et al. \(2020\)](#). This method estimates the scale length and the scale height of the observed disk. In Fig. 3.11, we show the model surface brightness distribution of NGC 551 in edge-on orientation in the left panel and a 2D fit to it in the middle panel. We also show the residual in the right panel of the figure. As can be seen, the edge-on surface brightness is fitted well by the 2D function. We find the scale length of the stellar disk to be ~ 3.2 kpc. However, the scale length of the stellar disk in NGC 551 is ~ 4.6 kpc (from an exponential fitting to the surface density profile derived using $3.6 \mu\text{m}$ data), which is considerably different. This indicates that at edge-on orientation, due to the line-of-sight integration effect, a 2D fit does not recover the true scale length of the disk. From the 2D fit, the scale height of the stellar disk was found to be ~ 400 pc, which reasonably matches with the actual scale height (it varies between $200 - 470$ pc as seen in Fig. 3.3).

Although the recovered scale height matches the actual values reasonably, an underestimated scale length can significantly affect the computed flattening ratio. For NGC 551, the actual flattening ratio is calculated using the stellar scale height (Fig. 3.3) and the measured scale length (4.6 kpc). This flattening ratio

is shown in Fig. 3.12 as a function of radius. As can be seen, the flattening ratio varies between $\sim 10 - 23$ within the galaxy. This ratio is much different than the values reported in the literature for other galaxies. For example, Reshetnikov et al. (2019) used the surface brightness of edge-on galaxies to investigate the dependence of the flattening ratio on galaxy luminosity. They found the ratio to vary between $\sim 4.6 - 5.3$ within their sample. Similarly, several studies have also investigated the flattening ratio in the I-band and found it to vary between $5 - 10$ depending on galaxy types and other properties (Kregel et al., 2002).

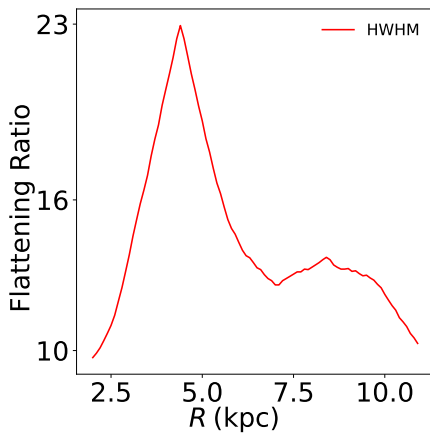


Figure 3.12: The estimated flattening ratio of the stellar disk in NGC 551 as a function of radius. The estimation was done using the modeled scale height and the observed scale length of the disk. As can be seen, the flattening ratio varies substantially (between $\sim 10 - 23$) with radius.

These studies estimated the flattening ratios by fitting the edge-on stellar surface densities. As we have seen above, these fittings can severely underestimate the disk scale length. As a result, it can underestimate the flattening ratios. For NGC 551, the calculated flattening ratio using the fitted values is ~ 7.1 . This is consistent with the literature but much lower than the actual value (between $10 - 23$). This indicates that the line-of-sight integration effect significantly biases the deduced structure of the stellar disks. Detailed modeling provides a much clearer insight into the three-dimensional distribution of stars in the stellar disks of galaxies.

We further investigate the perceived signature of multi-component disk by examining the vertical slices of the model edge-on surface brightness distribution of NGC 551. In Fig. 3.13, we plot vertical slices profiles at two different radii, i.e., 2.5 kpc and 3.5 kpc. We fit these vertical profiles with single (first and third panels) and double Gaussian (second and fourth panels) profiles. From the figure, it can be seen that in both the radii, a double Gaussian

fits the vertical profiles better than a single Gaussian. In the double Gaussian fit, the narrow component has a scale height of ~ 160 pc, whereas the broad component has a scale height of ~ 360 pc. This mimics the existence of a two-component stellar disk, while the model disk had only one component. Hence, the inference of the existence of two-component disks in galaxies by fitting the edge-on surface density distribution might be contaminated by projection effects.

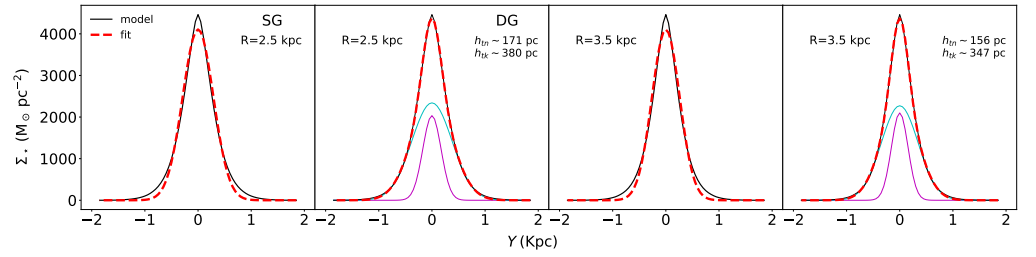


Figure 3.13: The vertical slices profile of the simulated intensity distribution of the stellar disk at an edge-on orientation, and its fit with single and double Gaussian components. The first two panels show vertical slices at a radius of 2.5 kpc, whereas the last two panels show cuts at 3.5 kpc. The solid black lines represent the vertical slices of the edge-on intensity. The dashed red lines represent the fits. The first and third panels show a single Gaussian fit, whereas the second and fourth panels represent a double Gaussian fit.

3.6 Plausible Formation Scenarios of Thick Stellar Disk

The double-component structure of stellar disks, comprising thin and thick components, was first proposed by [Gilmore & Reid \(1983\)](#). The subsequent decades have witnessed a large body of observational work providing evidence for contrasting disk attributes. The inquiry into the origin of the thick disk has been a hot topic of debate for a few decades now, with ex-situ mechanisms such as accretion of the stars (formed ex-situ) from disrupted satellite galaxies ([Abadi et al., 2003](#)) and in-situ processes involving kinematic heating. The in-situ processes can be attributed to various sources, which encompass radial migration induced by resonances ([Sellwood & Binney, 2002](#)), the dynamical impacts of bulges ([Saha et al., 2010](#)), interactions with Giant Molecular Clouds (GMCs) ([Fujimoto et al., 2023](#)), and the disruptive effects of stellar clumps ([Bournaud et al., 2009](#)).

In the galaxy NGC 551, by solving the combined Poisson equation, we obtained the density solution as a function of radius and height. The maximum height for the stellar disk varies from 830 pc to 1990 pc. The maximum height at the stellar scale length (l_*) of 4.6 kpc is ~ 1190 pc. To figure out which in-situ method can better explain the height observed, we compare the free fall time of stars with the secular time required by different in-situ mechanisms that facilitate vertical stellar displacements. This comparison helps us in our understanding of plausible formation methods for the thick disk and underscores a more viable mechanism for thick disk formation in the galaxy.

3.6.1 Radial Migration

It was first proposed by [Sellwood & Binney \(2002\)](#), who stated that the star birth radius will change over time due to perturbation in the plane or vertically causing an increase in epicycle known as blurring, which refers to orbital heating. The other method proposed is known as churning, which happens in the presence of non-axisymmetric patterns such as spiral arms that exert torque on stars, which leads to a change in angular momentum.

In the study conducted by [Vera-Ciro et al. \(2016\)](#), a comprehensive exploration into the ramifications of radial migration upon the vertical scale height of galaxies was undertaken. The simulations were executed on a model representing a light disk galaxy, a heavy disk, and a Milky Way-like galaxy involving a substantial assembly of 5 million discrete particles. We chose the Milky Way-like galaxy model from other different models due to its parameters being closest to those of NGC 551.

In their results, they have provided a graphical representation of three particles (stars) radial migration trajectories over time as well as the vertical displacement during this process; all three have a similar guiding center radius of 5 kpc. These particles exhibited distinctive behaviors: one displayed nominal secular evolution, another migrated radially inward, and the third migrated outward. Notably, the particle that abstained from substantial secular evolution exhibited the most pronounced vertical displacement, traversing a span from 0 to 1170 pc over a simulation interval of 2.5 billion years, whereas the particles migrating radially moved vertically up to 100 and 200 pc only.

Comparing the dynamical heating time due to radial migration with the free fall time from a height of 1190 pc to the midplane of the galaxy; 32Myr, suggests that the formation of the thick disk is not possible due to radial migration, which is consistent with other works (see, e.g., [Vera-Ciro et al., 2016](#)).

3.6.2 Bars

Galactic disks encompass a variety of non-axisymmetric patterns, including bars, spirals, and warps. Extensive research has been conducted in the scientific literature to understand whether these patterns contribute to the vertical heating of the stellar disk. In a study conducted by [Saha et al. \(2010\)](#), N-body simulations were employed across diverse models to investigate the correlation between the growth rate of bar potential and the vertical heating exponent. The obtained correlation was approximately 0.647. The study also examined the temporal aspect of vertical heating. The outer disk experienced a twofold change in vertical heating over approximately four billion years, while the central region encountered a threefold change in vertical heating over five to six billion years.

These timescales are comparable to or exceed ten revolutions of the galaxy. Due to the absence of hydrostatic equilibrium in the bar region, direct comparisons and inferences regarding our sample galaxy is not possible. However, given the considerable timescales involved, it is reasonable to assume that just the vertical heating induced by the bar is inadequate for the formation of a thick disk.

3.6.3 GMCs

The Giant Molecular Cloud (GMC) presents another potential mechanism for inducing vertical heating within the galactic disk, achieved through the gravitational scattering of stars resulting from collisions with GMCs (Lacey, 1984). Most of the previous investigations concerning GMCs have predominantly involved simulation runs spanning substantial temporal scales of approximately 10 billion years. In the study done by Fujimoto et al. (2023), they have carried out simulations covering a narrower timeframe of 1 billion years, affording a detailed examination of GMC dynamics within the initial few million years. Numerical analyses reveal that the temporal evolution of velocity dispersion can be suitably modeled by a power law $\sigma \propto t^\beta$ with $\beta > 1$ for the first few million years and then for the following years it varies between 0.3 and 0.7. The study obtains the time evolution of normalized cumulative distribution functions for local height maxima of tracer particles, initialized with a radius of 6 kpc and a height of 0 pc. From the derived graph, it is established that the stars attain a maximum altitude of 320 pc within a span of 1.05 billion years. Comparing this timescale with the calculated free fall time of 32 million years, a compelling assertion emerges: GMCs in isolation cannot provide energy for the formation of a thick disk.

3.6.4 Stellar Clumps

In the study done by Bournaud et al. (2009) and further expanded upon by Qu et al. (2011), a comprehensive analysis was conducted using N-body+Smooth Particle hydrodynamics simulation to study the secular evolution occurring due to stellar clumps. These clumps were characterized by masses on the order

of a few $10^8 M_{\odot}$. A significant observation arising from these simulations is the transitory nature of these clumps in a galaxy's evolutionary timeline. In numerous simulations, these clumps were observed to dissipate or migrate towards the galactic center to contribute to bulge formation, ultimately being a prominent feature only in the early stages of galactic evolution, with their presence diminishing approximately 4 billion years into the simulation. In the subsequent investigation by [Qu et al. \(2011\)](#), they ran the simulation for 3 billion years, where they got the result of constant scale height across a radius of $Z \sim 0.85$ kpc. When contrasted with our findings, which reveal a scale height variation from a minimum of 200 pc to a maximum of 470 pc, it becomes apparent that stellar clumps may not possess the requisite energy to impart stars with the observed vertical heights.

Chapter 4

Conclusions and Scope for Future Work

We have assumed the galactic disk in NGC 551 to be a multi-component system consisting of stellar, atomic, and molecular disks in vertical hydrostatic equilibrium under their mutual gravity in the external force field of the dark matter halo. We set up the corresponding joint Poisson's equations of vertical hydrostatic equilibrium and solved them numerically to obtain a three-dimensional density distribution in the stellar disk.

The stellar vertical velocity dispersion (σ_*) plays a crucial role in determining the structure of the stellar disk under the vertical hydrostatic equilibrium. The σ_* decides the vertical pressure in the disk, which balances the gravity of the disk. Observationally determining the σ_* had been difficult until recently. Almost all previous studies aimed at hydrostatic modeling of the galactic disk calculated σ_* analytically, considering the stellar disk to be an isolated single-component system in vertical hydrostatic equilibrium under solely its own gravity. However, in this study, for NGC 551, we used IFU observations from the CALIFA survey and estimated the σ_* .

The observed σ_* is the intensity-weighted velocity dispersion, MOM2, along a line-of-sight. We use an iterative method to consistently solve the hydrostatic equilibrium equations, starting from MOM2 as input to recover the correct σ_* . At the end of this method, we recover a σ_* profile, which consistently produces the observed MOM2 profile in a simulated observation. We find that this stellar

velocity dispersion is very different from the analytically calculated one. For NGC 551, the intrinsic velocity dispersion can differ from the analytically calculated value as significantly as by 70%.

The solutions of the hydrostatic equilibrium equation provide the three-dimensional density distribution in the stellar, atomic, and molecular disks. For NGC 551, we solve the equations at $2 \leq R \leq 11$ kpc every 100 pc. We find that the vertical density distribution at all radii for all the components (stars, atomic, and molecular gas) considerably depends on the assumed σ_* . Our estimated density distribution at the midplane using IFU data (instead of using the analytical expression for σ_*) can differ by 91% for the stellar disk and by 25% and 22% in the atomic and molecular disks, respectively.

We estimate the scale heights (HWHM) in the stellar and gas disks in NGC 551 using the derived density solutions. We find the stellar scale height to vary between 200 - 470 pc. The stellar and the gas disks are found to flare as a function of radius. We find that the analytically calculated σ_* overestimates the scale height in NGC 551 by about a factor of two. This is concerning as it can artificially increase the thickness of the stellar disk by a large amount, creating a thick disk. Hence, using correct stellar velocity dispersion estimated by spectroscopic observation is critical in determining vertical scale height in stellar disks.

We use density solutions and the observed rotation curve to build a three-dimensional dynamical model of the stellar disk in NGC 551. This model is then inclined to the observed inclination and projected into the sky plane to produce model spectral cube and moment maps. These moment maps are observationally equivalent. We compare the simulated moment zero map (surface brightness distribution) with the observed one by taking vertical slices along the minor axis of the disk. Our model vertical slices match the observation largely, except at the central region close to the midplane. We find an extra sharp feature/spike at the central region of the IFU and $3.6 \mu\text{m}$ cuts, which is not present in the model. This feature is more prominent in the IFU data than in the $3.6 \mu\text{m}$ data. We further compared the vertical slices of the moment zero map of thick + thin and thick + bar models. The thick + thin model cut matched with the IFU

observation with $\sigma_{*,\text{tn}}$ of 6 and 7 km s⁻¹ for the models respectively. However, the thick + bar model cut was still not able to produce the high peaks as seen in the IFU cut but matched with the Spitzer 3.6 μm . This strengthens the idea that the higher peak could be an indication of the thin disk in NGC 551.

Next, we investigate how the stellar disk in NGC 551 would be observed in edge-on orientation. We incline our dynamical model to an inclination of 90° and project it into the sky plane. Using the traditional method used in the literature, we fit this edge-on intensity distribution with the modified Bessel function of the first kind ($K(x)$) and sech^2 . We find that this projection and fitting can artificially reduce the scale length of the stellar disk. Consequently, the estimated observed flattening ratio can also be decreased significantly. For NGC 551, the fitted flattening ratio is calculated to be ~ 7.1 , whereas its actual ratio varies between 10 – 23. Hence, estimating the structural parameters of stellar disks by simply 2D-fitting the edge-on surface density might be corrupted by line-of-sight integration effects.

We further examine the vertical slices profiles of the edge-on model disk in NGC 551 to investigate multi-component disks. We found that a Double Gaussian fitted the vertical profiles better than a single Gaussian. This indicates that even a single-component disk can be perceived as a two-component one due to the line-of-sight integration effect in edge-on orientation. Hence, the conclusion of the existence of two-component disks in external galaxies by fitting the surface densities of edge-on galaxies might be contaminated, and detailed modeling could provide more insight into the three-dimensional structure of the stellar disks in galaxies.

We have performed the dynamical modeling in NGC 551 to understand the existence of a multi-component stellar disk. However, to understand several physical properties in more detail, a statistically significant sample is required. To address this, we plan to perform a similar analysis to a large number of galaxies from the CALIFA survey. This would provide a clear picture of the existence of multi-component stellar disks in external galaxies.

Bibliography

- Abadi M. G., Navarro J. F., Steinmetz M., Eke V. R., 2003, [ApJ](#) , 597, 21
- Anders F., Chiappini C., Santiago B. X., Matijević G., Queiroz A. B., Steinmetz M., Guiglion G., 2018, [A&A](#) , 619, A125
- Andrae R., et al., 2018, [A&A](#) , 616, A8
- Bacon R., et al., 2010, in Ground-based and Airborne Instrumentation for Astronomy III. pp 131–139
- Banerjee A., Jog C. J., 2007, [ApJ](#) , 662, 335
- Banerjee A., Jog C. J., Brinks E., Bagetakos I., 2011, [MNRAS](#) , 415, 687
- Bensby T., Feltzing S., 2006, [MNRAS](#) , 367, 1181
- Bensby T., Alves-Brito A., Oey M. S., Yong D., Meléndez J., 2011, [ApJL](#) , 735, L46
- Bershady M. A., Verheijen M. A. W., Swaters R. A., Andersen D. R., Westfall K. B., Martinsson T., 2010a, [ApJ](#) , 716, 198
- Bershady M. A., Verheijen M. A. W., Westfall K. B., Andersen D. R., Swaters R. A., Martinsson T., 2010b, [ApJ](#) , 716, 234
- Biswas P., Patra N. N., Roy N., Rashid M., 2022, [MNRAS](#) , 513, 168
- Biswas P., Kalinova V., Roy N., Patra N. N., Tyulneva N., 2023, [MNRAS](#) , 524, 6213
- Bizyaev D. V., Kautsch S. J., Mosenkov A. V., Reshetnikov V. P., Sotnikova N. Y., Yablokova N. V., Hillyer R. W., 2014, [ApJ](#) , 787, 24

Bland-Hawthorn J., Gerhard O., 2016, [ARAA](#) , [54](#), [529](#)

Bock D. C. J., et al., 2006, in Stepp L. M., ed., Society of Photo-Optical Instrumentation Engineers (SPIE) Conference Series Vol. 6267, Ground-based and Airborne Telescopes. p. 626713, [doi:10.1117/12.674051](#)

Bolatto A. D., Wolfire M., Leroy A. K., 2013a, [ARAA](#) , [51](#), [207](#)

Bolatto A. D., et al., 2013b, [Nature](#) , [499](#), [450](#)

Bolatto A. D., et al., 2017, [ApJ](#) , [846](#), [159](#)

Bournaud F., Elmegreen B. G., Martig M., 2009, [ApJL](#) , [707](#), [L1](#)

Bovy J., Rix H.-W., Schlafly E. F., Nidever D. L., Holtzman J. A., Shetrone M., Beers T. C., 2016, [ApJ](#) , [823](#), [30](#)

Brandt J. C., 1960, [ApJ](#) , [131](#), [293](#)

Brook C. B., et al., 2012, [MNRAS](#) , [426](#), [690](#)

Buder S., et al., 2018, [MNRAS](#) , [478](#), [4513](#)

Bundy K., et al., 2014, [ApJ](#) , [798](#), [7](#)

Caldú-Primo A., Schrubba A., Walter F., Leroy A., Sandstrom K., de Blok W. J. G., Ianjamasimanana R., Mogotsi K. M., 2013, [AJ](#) , [146](#), [150](#)

Cappellari M., 2002, [MNRAS](#) , [333](#), [400](#)

Cappellari M., 2020, [MNRAS](#) , [494](#), [4819](#)

Cappellari M., et al., 2011, [MNRAS](#) , [413](#), [813](#)

Chakraborty A., Roy N., 2024, in 42nd meeting of the Astronomical Society of India (ASI. p. I01

Cid Fernandes R., et al., 2013, [A&A](#) , [557](#), [A86](#)

Ciučă I., Kawata D., Miglio A., Davies G. R., Grand R. J. J., 2021, [MNRAS](#) , [503](#), [2814](#)

Combes F., Becquaert J. F., 1997, [A&A](#) , 326, 554

Comerón S., et al., 2011a, [ApJ](#) , 729, 18

Comerón S., et al., 2011b, [ApJ](#) , 741, 28

Comerón S., Salo H., Knapen J. H., 2018, [A&A](#) , 610, A5

Croom S. M., et al., 2021, [MNRAS](#) , 505, 991

Cuomo V., Lopez Aguerri J. A., Corsini E. M., Debattista V. P., Méndez-Abreu J., Pizzella A., 2019, [A&A](#) , 632, A51

De Geyter G., Baes M., Camps P., Fritz J., De Looze I., Hughes T. M., Viaene S., Gentile G., 2014, [MNRAS](#) , 441, 869

Elia D., et al., 2022, [ApJ](#) , 941, 162

Emsellem E., Monnet G., Bacon R., 1994, [A&A](#) , 285, 723

Eskew M., Zaritsky D., Meidt S., 2012, [ApJ](#) , 143, 139

Feast M. W., Menzies J. W., Matsunaga N., Whitelock P. A., 2014, *Nature*, 509, 342

Fox E. P., 1998, *Data analysis: a Bayesian tutorial*

Freedman W. L., 2021, [ApJ](#) , 919, 16

Friedmann A., 1999, [General Relativity and Gravitation](#), 31, 1991

Fuhrmann K., 1998, [A&A](#) , 338, 161

Fujimoto Y., Inutsuka S.-i., Baba J., 2023, [MNRAS](#) , 523, 3049

Gadotti D. A., 2008, [MNRAS](#) , 384, 420

Gaia Collaboration et al., 2021a, [A&A](#) , 649, A1

Gaia Collaboration et al., 2021b, [A&A](#) , 649, A6

Gilmore G., Reid N., 1983, [MNRAS](#) , 202, 1025

Gilmore G., et al., 2022, [A&A](#) , 666, A120

Goodwin S. P., Gribbin J., Hendry M. A., 1998, The Observatory, [118](#), 201

Grand R. J. J., et al., 2020, [MNRAS](#) , 497, 1603

Hodge P. W., 1983, [PASP](#) , 95, 721

Imig J., et al., 2023, [ApJ](#) , 954, 124

Irwin J. A., Sofue Y., 1996, [ApJ](#) , 464, 738

Ivezić Ž., et al., 2008, [ApJ](#) , 684, 287

Jing Y. P., Suto Y., 2000, [ApJL](#) , 529, L69

Jog C. J., Narayan C. A., 2001, [MNRAS](#) , 327, 1021

Jurić M., et al., 2008, [ApJ](#) , 673, 864

Kalberla P. M. W., Kerp J., Dedes L., Haud U., 2014, [ApJ](#) , 794, 90

Kamphuis J., Sancisi R., 1993, [A&A](#) , 273, L31

Kamphuis P., Józsa G. I. G., Oh S. . H., Spekkens K., Urbancic N., Serra P., Koribalski B. S., Dettmar R. J., 2015, [MNRAS](#) , 452, 3139

Kregel M., van der Kruit P. C., de Grijs R., 2002, [MNRAS](#) , 334, 646

Lacerda E. A., Sánchez S., Mejía-Narváez A., Camps-Fariña A., Espinosa-Ponce C., Barrera-Ballesteros J., Ibarra-Medel H., Lugo-Aranda A., 2022, [New Astronomy](#), 97, 101895

Lacey C. G., 1984, [MNRAS](#) , 208, 687

Larsen J. A., Humphreys R. M., 2003, [AJ](#) , 125, 1958

Lee Y. S., et al., 2011, [ApJ](#) , 738, 187

Leroy A. K., Walter F., Brinks E., Bigiel F., de Blok W. J. G., Madore B., Thornley M. D., 2008, [AJ](#) , 136, 2782

Lewis J. R., Freeman K. C., 1989, [AJ](#) , 97, 139

- Lian J., et al., 2022, [MNRAS](#) , 513, 4130
- López-Cobá C., Sánchez S. F., Bland-Hawthorn J., Moiseev A. V., Cruz-González I., García-Benito R., Barrera-Ballesteros J. K., Galbany L., 2019, [MNRAS](#) , 482, 4032
- López-Cobá C., et al., 2020, [AJ](#) , 159, 167
- López-Corredoira M., Molgó J., 2014, [A&A](#) , 567, A106
- López-Corredoira M., Cabrera-Lavers A., Garzón F., Hammersley P. L., 2002, [A&A](#) , 394, 883
- Luo A. L., et al., 2015, [Research in Astronomy and Astrophysics](#), 15, 1095
- Mackereth J. T., et al., 2017, [MNRAS](#) , 471, 3057
- Mackereth J. T., et al., 2019, [MNRAS](#) , 489, 176
- Majewski S. R., et al., 2017, [AJ](#) , 154, 94
- Makarov D., Prugniel P., Terekhova N., Courtois H., Vauglin I., 2014, [A&A](#) , 570, A13
- Marasco A., Fraternali F., van der Hulst J. M., Oosterloo T., 2017, [A&A](#) , 607, A106
- Mateu C., Vivas K., Downes J. J., Briceño C., Cruz G., 2012, in European Physical Journal Web of Conferences. p. 04006, [doi:10.1051/epjconf/20121904006](#)
- Meidt S., et al., 2013, Uncovering Dark Matter in Galaxies Across the Hubble Sequence, Spitzer Proposal ID 10096
- Meidt S. E., et al., 2014, [ApJ](#) , 788, 144
- Miglio A., et al., 2021, [A&A](#) , 645, A85
- Mogotsi K. M., de Blok W. J. G., Caldú-Primo A., Walter F., Ianjamasimanana R., Leroy A. K., 2016, [AJ](#) , 151, 15

Momany Y., Zaggia S., Gilmore G., Piotto G., Carraro G., Bedin L. R., de Angeli F., 2006, [A&A](#) , 451, 515

Monnet G., Bacon R., Emsellem E., 1992, [A&A](#) , 253, 366

Moore B., Governato F., Quinn T., Stadel J., Lake G., 1998, [ApJL](#) , 499, L5

Mosenkov A., et al., 2020, [MNRAS](#) , 494, 1751

Mosenkov A. V., Savchenko S. S., Smirnov A. A., Camps P., 2021, [MNRAS](#) , 507, 5246

Muñoz-Mateos J. C., et al., 2015, [ApJS](#) , 219, 3

Narayan C. A., Jog C. J., 2002, [A&A](#) , 394, 89

Navarro J. F., Frenk C. S., White S. D. M., 1997, [ApJ](#) , 490, 493

Ness M., Hogg D. W., Rix H. W., Martig M., Pinsonneault M. H., Ho A. Y. Q., 2016, [ApJ](#) , 823, 114

Nidever D. L., et al., 2014, [ApJ](#) , 796, 38

Pahre M. A., Ashby M. L. N., Fazio G. G., Willner S. P., 2004, [ApJS](#) , 154, 235

Patra N. N., 2019, [MNRAS](#) , 484, 81

Patra N. N., 2020, [MNRAS](#) , 499, 2063

Patra N. N., 2021, [MNRAS](#) , 501, 3527

Peters S. P. C., de Geyter G., van der Kruit P. C., Freeman K. C., 2017, [MNRAS](#) , 464, 48

Pinsonneault M. H., et al., 2018, [ApJS](#) , 239, 32

Qu Y., Matteo P. D., Lehnert M. D., van Driel W., 2011, [A&A](#) , 530, A10

Reddy B. E., Lambert D. L., Allende Prieto C., 2006, [MNRAS](#) , 367, 1329

Reshetnikov V. P., Usachev P. A., Savchenko S. S., 2019, [Astronomy Letters](#) , 45, 565

Robin A. C., Reyl   C., Fliri J., Czekaj M., Robert C. P., Martins A. M. M., 2014, [A&A](#) , 569, A13

Robin A. C., et al., 2022, [A&A](#) , 667, A98

Rogstad D. H., Lockhart I. A., Wright M. C. H., 1974, [ApJ](#) , 193, 309

Saha K., Tseng Y.-H., Taam R. E., 2010, [ApJ](#) , 721, 1878

S  nchez S. F., et al., 2012, [A&A](#) , 538, A8

S  nchez S. F., et al., 2016a, [RMxAA](#) , 52, 171

S  nchez S. F., et al., 2016b, [A&A](#) , 594, A36

Sarkar S., Jog C. J., 2020, [MNRAS](#) , 499, 2523

Sattler N., Pinna F., Neumayer N., Falc  n-Barroso J., Martig M., Gadotti D. A., van de Ven G., Minchev I., 2023, [MNRAS](#) , 520, 3066

Sellwood J. A., Binney J. J., 2002, [MNRAS](#) , 336, 785

Serra P., et al., 2015, [MNRAS](#) , 448, 1922

Sheth K., et al., 2010, [PASP](#) , 122, 1397

Shostak G. S., van der Kruit P. C., 1984, [A&A](#) , 132, 20

Skrutskie M. F., et al., 2006, [AJ](#) , 131, 1163

Snaith O. N., Haywood M., Di Matteo P., Lehnert M. D., Combes F., Katz D., G  mez A., 2014, [ApJL](#) , 781, L31

Soubiran C., Bienaym   O., Siebert A., 2003, [A&A](#) , 398, 141

Springob C. M., Masters K. L., Haynes M. P., Giovanelli R., Marinoni C., 2007, [ApJS](#) , 172, 599

Stark A. A., 1984, [ApJ](#) , 281, 624

Steinmetz M., et al., 2020, [AJ](#) , 160, 82

- Swarup G., Ananthakrishnan S., Kapahi V. K., Rao A. P., Subrahmanya C. R., Kulkarni V. K., 1991, *Current Science*, **60**, 95
- Vera-Ciro C., D’Onghia E., Navarro J. F., 2016, *ApJ* , **833**, 42
- Vieira K., Carraro G., Korchagin V., Lutsenko A., Girard T. M., van Altena W., 2022, *ApJ* , **932**, 28
- Walcher C. J., et al., 2014, *A&A* , **569**, A1
- Wu Y., et al., 2019, *MNRAS* , **484**, 5315
- Yoachim P., Dalcanton J. J., 2006, *AJ* , **131**, 226
- Yusifov I., 2004, in Uyaniker B., Reich W., Wielebinski R., eds, *The Magnetized Interstellar Medium*. pp 165–169 ([arXiv:astro-ph/0405517](https://arxiv.org/abs/astro-ph/0405517)), [doi:10.48550/arXiv.astro-ph/0405517](https://doi.org/10.48550/arXiv.astro-ph/0405517)
- de Vaucouleurs G., de Vaucouleurs A., Corwin Herold G. J., Buta R. J., Paturel G., Fouque P., 1991, *Third Reference Catalogue of Bright Galaxies*
- van den Bergh S., 1999, *A&ARv* , **9**, 273
- van der Kruit P. C., 1988, *A&A* , **192**, 117
- van der Kruit P. C., Searle L., 1981, *A&A* , **95**, 105